

# Polarization and Delivery System for Xenon-129

Thesis by  
Jaideep Singh

In Partial Fulfillment of the Requirements  
for the Degree of  
Bachelor of Science



California Institute of Technology  
Pasadena, California

2000

(Submitted May 15, 2000)

© 2000

Jaideep Singh

All rights Reserved

## Acknowledgements

First and foremost, I would like to thank Prof. Emlyn Hughes and Dr. Dave Pripstein for allowing me to be a member of their research group for 2.5 yrs. They have given me an unique opportunity to be involved in research which has both pure physics and practical implications. None of this work could have been accomplished without their advice and constant guidance. I have to thank Rick Gerhart for his expert glassblowing. Thanks must go to the group - particularly Nick, Clayton, Mark, and Steffen. I could not have made it this far without their help, encouragement, and brute force efforts. I must also thank my friends Alan, Kevin, Matt, Selwyn, and Bird whose constant support helped me make it through four *long* years at Caltech. Finally I wish to thank my family for their encouragement of my interest in science and their unconditional love & support regardless of my chosen endeavor.

## **Polarization and Delivery System for Xenon-129**

by

Jaideep Singh

In Partial Fulfillment of the  
Requirements for the Degree of  
Bachelor of Science

### **Abstract**

Magnetic Resonance Imaging (MRI) relying on the thermal polarization of water protons has limitations in tissues with low water densities and provides relatively low contrast images because of the small chemical shifts experienced by protons. Hyperpolarized noble gases, particularly Xenon-129, can overcome these difficulties with additional benefits. Noble gases are polarized by using the principles of optical pumping and spin exchange. This method was originally refined and developed for the preparation of polarized Helium-3 targets used in neutron spin structure experiments. My goals are to design and test a system capable of producing large volumes of highly polarized Xenon-129. This is being done in conjunction with an imaging collaboration with Prof. Scott Fraser of the Beckman Institute at Caltech. I have (1) demonstrated a cell design capable of being reused and producing large volumes of polarized Xenon-129, (2) built and tested a gas system capable of filling cells and characterizing & removing contaminants, (3) demonstrated pre-delivery polarizations as high as 5%, (4) demonstrated a successful delivery of polarized gas (about 0.05%) in the Fraser MRI Lab, and (5) initiated studies involving frozen Xenon delivery.

# Contents

<b>1</b>	<b>Introduction</b>	<b>1</b>
1.1	Overview . . . . .	1
1.2	Motivation . . . . .	1
1.2.1	Polarization Levels . . . . .	1
1.2.2	Tissues with Low Water Densities . . . . .	2
1.2.3	Chemical Shifts . . . . .	3
1.2.4	Other Considerations . . . . .	4
1.3	History . . . . .	4
1.4	Goals . . . . .	5
<b>2</b>	<b>Spin Polarization &amp; Spin Relaxation Mechanisms</b>	<b>7</b>
2.1	Overview . . . . .	7
2.2	Optical Pumping . . . . .	8
2.2.1	Basic Process . . . . .	8
2.2.2	Spin Temperature Distribution . . . . .	10
2.3	Spin Relaxation of <i>Rb</i> . . . . .	12
2.3.1	<i>Rb-X</i> Collisions . . . . .	12
2.3.2	Wall Collisions and Field Inhomogeneities . . . . .	13
2.4	Spin Exchange . . . . .	14
2.4.1	Polarization Transfer . . . . .	14
2.4.2	Frequency Shift . . . . .	16
2.5	Spin Relaxation of <i>Xe</i> . . . . .	16

<b>3</b>	<b>System Design &amp; Function</b>	<b>18</b>
3.1	Overview . . . . .	18
3.2	Materials Considerations . . . . .	18
3.3	Cells . . . . .	20
3.3.1	Design . . . . .	20
3.3.2	Components . . . . .	20
3.3.3	Preparation . . . . .	22
3.4	Gas System . . . . .	23
3.4.1	Contamination Removal . . . . .	24
3.4.2	Contamination Characterization . . . . .	24
3.4.3	Cell Filling . . . . .	26
3.5	Optical System . . . . .	27
3.5.1	Overview . . . . .	27
3.5.2	Pressure Broadening of <i>Rb</i> Absorption Lines . . . . .	28
3.5.3	Laser Systems . . . . .	29
3.5.4	Coils . . . . .	30
3.6	Delivery Mechanisms . . . . .	31
3.6.1	Gaseous Delivery . . . . .	32
3.6.2	Frozen <i>Xe</i> Delivery . . . . .	34
<b>4</b>	<b>Signal Measurement &amp; Data Analysis</b>	<b>35</b>
4.1	Overview . . . . .	35
4.2	NMR AFP . . . . .	36
4.2.1	Overview . . . . .	36
4.2.2	Description . . . . .	36
4.2.3	AFP Conditions . . . . .	37
4.2.4	Experimental Setup . . . . .	38
4.3	Pulsed NMR . . . . .	39
4.4	Calibration . . . . .	40
4.4.1	Thermal Water Proton Polarization . . . . .	40
4.4.2	Thermal Xenon Polarization . . . . .	44

4.5	Results of Polarization Measurements by AFP . . . . .	45
4.6	Results of Polarization Measurements by Pulsed NMR . . . . .	46
<b>5</b>	<b>Conclusion</b>	<b>50</b>
5.1	Overview . . . . .	50
5.2	Discussion of the Polarization Experiments . . . . .	50
5.3	Future Areas of Research . . . . .	52
5.3.1	Cell Wall Coatings . . . . .	52
5.3.2	<i>Cs</i> Spin Exchange . . . . .	52
5.3.3	Improvement of Materials . . . . .	53
5.3.4	Other Considerations . . . . .	54
<b>A</b>	<b>Constant &amp; Parameter Data Sheet</b>	<b>55</b>
<b>B</b>	<b>Magnetic Resonance</b>	<b>57</b>
B.1	Time Evolution of Spins in Static & Rotating Fields . . . . .	57
B.2	Effective Field Felt by a Spin . . . . .	59
B.3	Signal Induced by Spin Flip . . . . .	61
<b>C</b>	<b>Dynamics of <i>Xe</i> in a Biological Environment</b>	<b>64</b>
C.1	Overview . . . . .	64
C.2	Delivery by Ventilation . . . . .	64
C.3	Delivery by Injection . . . . .	65
C.4	<i>Xe</i> Uptake Models . . . . .	66
C.5	Relaxation in Various Tissues . . . . .	66

## List of Figures

2.1	Ground State Energy Level Diagram for Rb-85. The hyperfine and Zeeman splittings are depicted for small magnetic fields. . . . .	9
2.2	Optical Pumping for the Case $I=0$ . The incident photons have angular momentum of $+1$ ; therefore, the electrons are excited to the $m=+1/2$ state. . . . .	10
3.1	Glass Cell with Teflon Valve. The diameter and length of the cell are both 2". . . . .	21
3.2	Gas System Schematic. . . . .	23
3.3	RGA Scan Before Bake. The peaks are (in order of size) 18,17-Water, 1-Hydrogen, 28-Nitrogen, 44-Carbon Dioxide, and 32-Oxygen . . . .	25
3.4	RGA Scan After Bake. The peaks are (in order of size) 1-Hydrogen, 18,17,16-Water, 28-Nitrogen, 44-Carbon Dioxide, and 32-Oxygen. . .	26
3.5	Optical Setup. The cell is being pumped from both windows using the 150 W LDA. . . . .	28
3.6	LDA Emission Spectrum. . . . .	30
3.7	Magnified Beam Profile. This is a typical beam profile of a 30 W LDA. Note the spatial distribution of photons in the beam. . . . .	31
3.8	Delivery Line Scematic. The cell is sitting in the coils and the probe is inserted into the pick up coils for measurement. . . . .	32
4.1	AFP Sweep. Time increases alphabetically. The spin is precessing about the effective B field. . . . .	37

4.2	AFP Electronic Apparatus. The apparatus also includes a sweep generator (not pictured) that is connected to the coil creating the holding field. . . . .	39
4.3	Q Curve of the Pickup Coils used for AFP. The x-axis is the frequency in Hz and the y-axis is the response in arb. units. . . . .	42
4.4	First AFP Signal. There are two peaks because the field is swept through resonance twice. . . . .	45
4.5	Thermal Xenon Signal (24k avg). The signal is seen above the white arrow. . . . .	48
4.6	Hyperpolarized Xenon Signal (24 avg). This peak is distinguished from the thermal peak by (1) its narrower width and (2) its higher SNR. . . . .	48

## List of Tables

3.1	Magnetic Susceptibilities in cgs units of inverse megamol . . . . .	19
4.1	Typical AFP Polarization Parameters . . . . .	46
4.2	Pulsed NMR Measurement Parameters . . . . .	47
5.1	Comparison of Spin Exchange Parameters for Rb and Cs . . . . .	53
A.1	Parameters Relevant to Optical Pumping and Spin Exchange . . . . .	56
A.2	Pressure Conversions . . . . .	56
A.3	Nuclear Data of Relevant Elements . . . . .	56
C.1	Injectable Carrier Parameters . . . . .	65
C.2	Relaxation Times . . . . .	67

# Chapter 1

## Introduction

### 1.1 Overview

Magnetic resonance (MR) imaging and spectroscopy have become very powerful analytical tools in biomedicine over the past 20 years. Current magnetic resonance imaging (MRI) technology takes advantage of dense populations of protons readily found in the body as water. However, imaging thermally polarized water protons has some limitations. (1) Thermal polarization levels are relatively low. (2) Imaging tissues with low water densities is difficult. (3) Because of its small chemical shifts, water protons provide low contrast images of similar tissues. All of these limitations are overcome with hyperpolarized noble gases  $^{129}\text{Xe}$  and  $^3\text{He}$ , originally used as targets in high energy scattering experiments. In the following sections, each of these limitations and additional considerations are explored in more detail, a brief historical sketch of polarized noble gases is presented, and finally my goals for this thesis are described.

### 1.2 Motivation

#### 1.2.1 Polarization Levels

The level of thermal polarization of  $^1\text{H}$  is derived from the thermal equilibrium Boltzmann distribution, where  $\gamma$  is the gyromagnetic ratio of  $^1\text{H}$ :

$$P_{1H} = \frac{|N_{\uparrow} - N_{\downarrow}|}{N_{\uparrow} + N_{\downarrow}} = \tanh\left(\frac{\gamma\hbar B}{2kT}\right) \approx \frac{\gamma\hbar B}{2kT} \quad (1.1)$$

The two limiting factors in  $^1H$  thermal polarization are the magnitude of the magnetic field  $B$  and the temperature of the sample  $T$ . The  $B$ -field is both a financial and physical limitation. Superconducting magnets used in the imaging of small animals have strengths up to 12 T, but for imaging of humans, field strengths are closer to 2 T. Temperature is greatly limited for MR imaging *in vivo*. Based on these limitations, the highest  $P_{1H}$  attainable under *ideal conditions* is on the order of  $10^{-5}$ , but typical values are around  $10^{-6}$ . Polarization levels of hyperpolarized noble gases  $P_{Hyp}$  can range from 0.01 to 0.40 under similar field and temperature conditions [33],[31]. This is an improvement of 3 to 5 orders of magnitude over any thermally polarized species ( $^1H$ ,  $^3He$ ,  $^{129}Xe$ ).

### 1.2.2 Tissues with Low Water Densities

Some tissues and organs are notoriously difficult to image because of their low water density. The standard example is the void space in the lungs which have low gaseous water densities. Void space imaging of the lungs can be and has been performed effectively using noble gases [1],[28]. For this application  $^3He$  is better suited than  $^{129}Xe$ . It can be shown that the magnitude of the signal detected (in pickup coils) has the form (see Appendix B):

$$S \propto \gamma^2 \rho P_{Hyp} \quad (1.2)$$

Higher polarization levels can be more easily achieved in  $^3He$ . Noise pickup (mainly Johnson noise) scales as  $\omega = \gamma B$ , thus signal to noise ratio (SNR) scales as  $\gamma$  in the same  $B$ -field. Since  $^3He$  has a  $\gamma$  of 2.74 times larger than that of  $^{129}Xe$ , its SNR is higher.  $Xe$  is an anesthetic and therefore must be used in concentrations of less than 35% [28]. Thus higher densities  $\rho$  of  $^3He$  can be used. Together

these factors easily result in SNRs an order of magnitude higher than  $^{129}\text{Xe}$  in void spaces. Other examples of tissues with low water densities are environments that are dense in lipids (long chains of hydrocarbons) which are hydrophobic (water repelling). Due to its large electron cloud,  $^{129}\text{Xe}$  has a major advantage over  $^3\text{He}$ , because this cloud makes  $\text{Xe}$  very lipophilic (attracted to lipids). Therefore  $^{129}\text{Xe}$  is well suited to image lipid-rich environments such as the brain [17].

### 1.2.3 Chemical Shifts

When a magnetic field  $B$  is applied to an atom, the electrons shield a fraction of the field  $B$  from the nucleus. The nucleus, therefore, sees an effective field of  $B^*$ . If the atom happens to be in the presence of another species of atoms, then the electron distribution about the nucleus may be pulled towards or away from the nucleus, consequently altering  $B^*$ . This is the chemical shift phenomenon and it is calculated by using a reference MR frequency:

$$\delta_{shift} = \frac{|\omega_{environment} - \omega_{ref}|}{\omega_{ref}} \cdot (10^6 \text{ppm}) \quad (1.3)$$

The reference frequency for  $^1\text{H}$  is the MR frequency of the protons in  $\text{Si}(\text{CH}_3)$ . Chemical shifts for  $^1\text{H}$  are generally due to electron clouds from neighboring atoms and range over 15 ppm in various tissues. Therefore differences in chemical shifts attributed to two different tissues are on the order of a few ppm. This relative insensitivity of  $^1\text{H}$  to its chemical environment leads to low contrast images and spectra.  $\text{Xe}$ 's large electron cloud gives it large chemical shifts which are on the order of hundreds of ppm (referenced from the gas phase MR frequency). Differences in chemical shifts are therefore on the order of tens of ppm which is much better than  $^1\text{H}$  [34].

### 1.2.4 Other Considerations

The only common link between most anesthetics is that they are lipophilic [3]. Thus, studying the mechanism of anesthetics, which is currently poorly understood, can be accomplished uniquely with  $Xe$ . Ironically, precisely because  $^1H$  is found readily in the body, there is always a background signal. This makes the isolation of particular tissues rather difficult. Alternatively,  $^{129}Xe$ , which is readily dissolved in lipid based solutions, can be injected directly into a particular target tissue [17]. Additionally  $^{129}Xe$  has diffusion rates into the bloodstream and subsequent tissues 10 to 30 times higher than  $^3He$  [8]. This in conjunction with the fact that there is no background  $Xe$  signal suggests the possibility of using hyperpolarized  $^{129}Xe$  in perfusion studies [23]. Interestingly enough  $^{133}Xe$  is used as a radioactive tracer, but it yields low SNRs. Unfortunately some forms of cosmic rays are the same as the radiation emitted by  $^{133}Xe$  which results in a high background signal.

## 1.3 History

In the late 60's, the first deep inelastic scattering experiments revealed that nucleons had point like constituents that accounted for only half of the nucleon spin. Experiments followed in the 70's and 80's using spin polarized targets to test the theoretical predictions of the Bjorken and Ellis-Jaffe Sum Rules. These early experiments were successful in determining the basic picture of spin structure. However, the neutron spin structure was inferred from proton and deuteron data, therefore the accuracy of the neutron spin structure was limited to the uncertainties of both the proton and deuteron measurements. Direct measurements of the neutron spin structure were made using polarized  $^3He$  as targets. Due to Pauli's exclusion principle, the spins of the two protons cancel in the ground state. Therefore the spin of  $^3He$  is attributable mainly ( $\approx 0.87$ ) to the spin of the neutron [11]. The principles of optical pumping and spin exchange are used to prepare large volumes of highly polarized  $^3He$  targets [27]. Optical Pumping was first demonstrated by Kastler in 1950 [22]. Ten years later it was discovered by Bouchiat et al. that  $Rb$  atoms

could spin exchange with  $^3\text{He}$  [7]. Later, Grover showed that  $\text{Rb-Xe}$  spin exchange is very efficient [18]. Experiments conducted at SLAC (led by my advisor Prof. Hughes) and those being continued at Jefferson National Lab (with whom we are collaborating) use hyperpolarized  $^3\text{He}$  as the target.

Since the mid 90's many of the groups originally involved in these spin structure experiments began to adapt these techniques for use in MRI. Albert et al. (Stony Brook/Princeton) first demonstrated hyperpolarized MRI in excised mouse lungs in 1994 [1]. In the few years afterwards, relaxation of noble gas polarization in blood was studied by various groups to determine the feasibility of *in vivo* imaging [2],[6]. Those studies revealed that the relaxation time of  $\text{Xe}$  in blood is highly dependant on the level of oxygenation. Meanwhile studies of the void space in lungs of mice was underway using both  $^3\text{He}$  and  $^{129}\text{Xe}$  [36],[38]. In 1997, Swanson et al. (Michigan) published the first image of the brain produced by hyperpolarized MRI [35]. They imaged the brain of a mouse which had been ventilated with polarized  $^{129}\text{Xe}$ . De Lange et al. (Virginia/Princeton) produced the first *in vivo* human lung image in 1996 [28]. In that same year, Kauczor et al. (Mainz, Germany) produced images of patients with and without respiratory problems [23]. They found that there are substantial defects in the images of those patients with problems. Goodson et al. (Berkeley) have proposed the use of injectable carriers of noble gases for MRI [17]. They have shown that relaxation times in blood can be increased by a factor of 20 by dissolving  $\text{Xe}$  into lipid based solutions. Martin et al. have developed a  $\text{Xe}$  uptake model [26]. Based on that model, it is predicted that at 2 T the proton SNR will be 50 times higher than the  $\text{Xe}$  SNR assuming an initial  $\text{Xe}$  polarization level of 0.5. A more detailed review of the current state of  $\text{Xe}$  delivery & uptake into biological environments can be found in Appendix C.

## 1.4 Goals

The goal of my thesis work is to develop a system of producing large volumes of highly polarized  $^{129}\text{Xe}$  in conjunction with an imaging collaboration with Prof.

Scott Fraser (Beckman Institute, Caltech). I have studied various aspects of polarization and delivery. Particular attention is paid to (1) the materials that come into contact with the polarized sample, (2) the cell used to hold the polarized sample, (3) the gas system used to prepare the cell and the sample, (4) the optical system used to polarize the sample, and (5) the delivery method used to transfer the polarized sample. Variants of the whole system are tested in our lab and in the Fraser MRI Lab in Beckman Institute.

In the following chapters, I discuss the principles of optical pumping and spin exchange. Relaxation, any process which causes the loss of spin polarization, mechanisms are described. Each component of the system is explored in detail. The different measurement and calibration methods are reviewed. I describe the two polarization experiments and give estimates of the polarization levels measured. Finally, I conclude with a discussion of the results and an enumeration of possible improvements & future studies.

## Chapter 2

# Spin Polarization & Spin Relaxation Mechanisms

### 2.1 Overview

The following chapter is an introduction to the theory of optical pumping and spin exchange. Angular momentum is transferred from circularly polarized light, tuned to the D1 transition, to alkali metal vapors, typically Rubidium, via optical pumping. Due to the conservation of angular momentum, electrons from only one of the two ground spin states are excited. The excited spin states are mixed through atomic collisions. Electrons return to either ground spin state via nonradiative quenching. Because of *Rb-Rb* collisions, the electrons settle into an equilibrium spin temperature distribution, with a majority of the electrons residing in a polarized state. The level of polarization of *Rb* is limited mainly by collisions with other atoms and wall relaxation. Through spin exchange, this non-equilibrium polarization is transferred to the nuclei of the noble gas. Because of the better spin exchange coupling between *Xe* and *Rb* than *He* and *Rb*, pumping times are orders of magnitude faster for *Xe* than for *He* (compare minutes to hours). The polarization level of *Xe* is limited mainly by the polarization level of *Rb*, *Xe-Xe* collisions, and wall relaxation. (Note that values of various parameters relating to optical pumping and spin exchange can be found in Appendix A.)

## 2.2 Optical Pumping

### 2.2.1 Basic Process

The first step in the polarization process is the optical pumping of *Rb*, which has two naturally occurring isotopes:  $^{85}\text{Rb}$  (72.2% natural abundance,  $I = \frac{5}{2}$ ) and  $^{87}\text{Rb}$  (27.8%,  $I = \frac{3}{2}$ ). The Hamiltonian of a *Rb* atom in a holding field  $\vec{B}$  is:

$$H = a \vec{I} \cdot \vec{S} + g\mu_B \vec{S} \cdot \vec{B} - \frac{\mu_I}{I} \vec{I} \cdot \vec{B} \quad (2.1)$$

(Note that the following convention is used:  $\vec{I}$  - *Rb* nuclear spin,  $\vec{S}$  - *Rb* electron spin,  $\vec{K}$  - *Xe* nuclear spin.) The first term is the hyperfine splitting which is due to the interaction between the nuclear and electron spins. The second and third terms are the Zeeman splitting terms of the electron and nuclear spin states. Since  $\mu_B \gg \mu_I$ , the Zeeman splitting is dominated by the electron spins. The magnetic field used for optical pumping is typically  $\approx 30$  gauss; therefore, the hyperfine splittings are larger than the Zeeman splittings, so the eigenstates of the Hamiltonian are also eigenstates of total angular momentum  $\vec{F} = \vec{I} + \vec{S}$  and its projection onto field axis  $m$ . The ground state energy level splittings of  $^{85}\text{Rb}$  are depicted in Fig. 2.1.

Let's first consider the case  $\vec{I} = 0$ . The D1 line ( $^2\text{S}_{\frac{1}{2}} \rightarrow ^2\text{P}_{\frac{1}{2}}$ ) of *Rb* is excited with circularly polarized light. The electron transitions must obey  $\Delta m = \pm 1$ , where  $m$  in this case is simply the z component of the electron spin. Since all of the incident radiation has angular momentum of either  $+\hbar$  or  $-\hbar$ , the valence electron is selectively excited out of one of the two ground spin states. The spin states in the excited level are mixed by collisions, so the the electron has an equal probability of decaying into either of the ground spin states. Energy is transferred from the electron to the rotational and vibrational modes of  $N_2$  molecules [5]. This allows the electrons to return to the ground state without releasing depolarizing radiation. In fact it has been calculated [31] that roughly only 5% of the atoms return to the ground state by the emission of a photon. The simple case of  $\vec{I} = 0$  is depicted in Fig. 2.2.

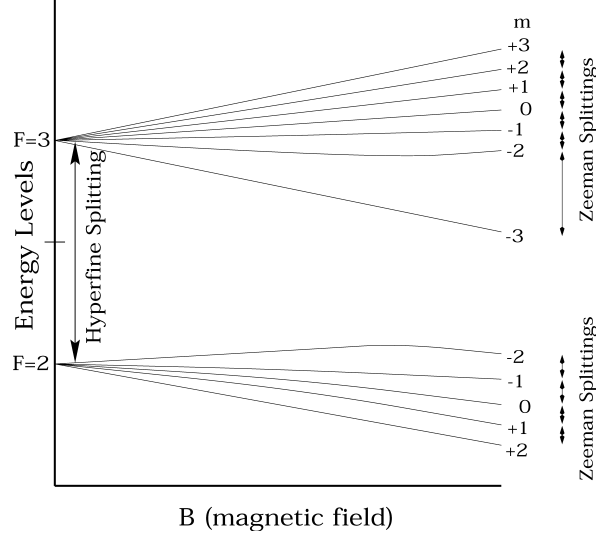


Figure 2.1: Ground State Energy Level Diagram for Rb-85. The hyperfine and Zeeman splittings are depicted for small magnetic fields.

In the case  $\vec{I} \neq 0$ , the atomic transitions must obey  $\Delta F = 0$  &  $\Delta m = \pm 1$  or  $\Delta F = \pm 1$  &  $\Delta m = 0$ , where  $F$  and  $m$  now refer to the total angular momentum which includes both the electron and nuclear spin. As the atoms are illuminated by polarized photons, each atom undergoes a series of spin state transitions until a spin state with no allowed transitions is reached. For example, with  $I = \frac{5}{2}$  and  $J_{photon} = +1$ , the final spin state is  $F = 3, m = 3$ .

The overall polarization of *Rb* achievable is given as a function of the optical pumping and spin relaxation rates:

$$P_{Rb} = \frac{\gamma_{OP}}{\gamma_{OP} + \frac{1}{T_{Rb}}} \quad (2.2)$$

$P_{Rb}$  typically reaches about 0.8 to 1.0 [40]. The optical pumping rate is given as:

$$\gamma_{OP} = \int \sigma(\nu) \Phi(\nu) d\nu \quad (2.3)$$

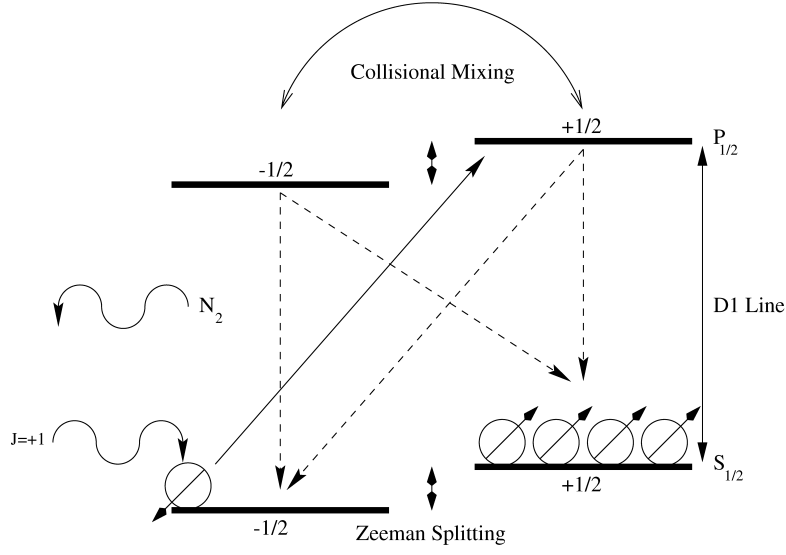


Figure 2.2: Optical Pumping for the Case  $I=0$ . The incident photons have angular momentum of  $+1$ ; therefore, the electrons are excited to the  $m=+1/2$  state.

where  $\sigma(\nu)$  is the light absorption cross section and  $\Phi(\nu)d\nu$  is the incident photon flux. Better matching between the absorption cross section and photon flux results in higher optical pumping rates. The relaxation rate is the sum of the relaxation rates from all the relaxation mechanisms:

$$\frac{1}{T_{Rb}} = \frac{1}{T_{Rb-Rb}} + \frac{1}{T_{Rb-N_2}} + \frac{1}{T_{Rb-Xe}} + \frac{1}{T_{wall}} + \frac{1}{T_{long}} + \frac{1}{T_{other}} \quad (2.4)$$

### 2.2.2 Spin Temperature Distribution

When a  $Rb$  atom undergoes a binary collision with another  $Rb$  atom, spin exchange occurs at a very efficient rate  $\approx 10^5 \frac{1}{s}$  [40]:



The interaction potential of the  $Rb$ - $Rb$  spin exchange is given as follows, where  $b(R)$

is electrostatic in nature and depends on the interatomic separation  $R$ :

$$V_{Rb-Rb} = b(R) \vec{S}_i \bullet \vec{S}_j \quad (2.5)$$

These collisions conserve total angular momentum  $F$  and are considered to be ‘sudden’ with respect to the nuclear spin polarization. Therefore only the electron spins are affected. During the collisions, the electron spins couple, dominating over the hyperfine interaction. Between collisions, however, the hyperfine interaction recouples the nuclear and electron spins causing a redistribution of angular momentum among the ground spin states, where  $\beta$  is the spin temperature and  $Z_j$  is the spin partition function:

$$\rho = \left( \frac{\exp(\beta S_z)}{Z_{S_z}} \right) \left( \frac{\exp(\beta I_z)}{Z_{I_z}} \right) \quad (2.6)$$

$Z_j$  is given as:

$$Z_j = \frac{\sinh\left(\beta\left(j + \frac{1}{2}\right)\right)}{\sinh\left(\frac{\beta}{2}\right)} \quad (2.7)$$

Given values for nuclear and electron spin,  $\beta$  is the only parameter that determines the spin distribution and it is related to the electron spin polarization as:

$$P_{Rb} = \tanh\left(\frac{\beta}{2}\right) \quad (2.8)$$

Therefore *each individual* spin exchange collision between  $Rb$  atoms does not affect the polarization, but an ensemble of *multiple* spin exchange collisions does result in limiting the level of polarization via electron randomization [40].

## 2.3 Spin Relaxation of *Rb*

### 2.3.1 *Rb-X* Collisions

The spin relaxation of *Rb* atoms comes mainly from *Rb-X* spin rotation interactions whose potential is given as:

$$V_{Rb-X} = \frac{2}{3}\lambda(R) \left[ 3 \left( \frac{\vec{R}}{R} \cdot (\vec{S}_i + \vec{S}_j) \right)^2 - 2 \right] + f(R) \vec{S} \cdot \vec{N}_{N_2} + \gamma(R) \vec{S} \cdot \vec{N} \quad (2.9)$$

The first term is theorized to be the form of the spin rotation coupling that causes relaxation by collisions between two polarized *Rb* atoms [5]. The component of total electron spin that is parallel to the internuclear axis between the two atoms is lost to the rotational angular momentum. This interaction is not well understood, but it is a major source of *Rb* spin relaxation. The relaxation rate due to *Rb-Rb* collisions is given as:

$$\frac{1}{T_{Rb-Rb}} = [Rb] \langle v\sigma \rangle_{Rb-Rb} \quad (2.10)$$

[*Rb*] is the concentration of *Rb* atoms and  $\langle v\sigma \rangle_{Rb-Rb}$  is the velocity averaged relaxation cross section. The second term is the coupling between the electron spin and the rotational angular momentum of a *Rb-N<sub>2</sub>* pair. Not many studies have been done of this interaction, but it is known that this interaction contributes little to the spin relaxation. The relaxation rate due to *Rb-N<sub>2</sub>* collisions is given as:

$$\frac{1}{T_{Rb-N_2}} = [N_2] \langle v\sigma \rangle_{Rb-N_2} \quad (2.11)$$

The last term is a similar coupling for a *Rb-Xe* pair, where most of the coupling originates from the noble gas core. This also is a major source of spin relaxation and

at high pressures it contributes as much spin relaxation as do the  $Rb-Rb$  interactions. The relaxation rate due to  $Rb-Xe$  collisions is given as:

$$\frac{1}{T_{Rb-Xe}} = [Xe] \langle v\sigma \rangle_{Rb-N_2} \quad (2.12)$$

A theoretical model for the spin rotation interaction between  $Rb$  and  $Xe$  developed by Wu et al. [45] yields:

$$\gamma(R) = \frac{m_e G}{MR} \frac{d|\phi_1(R)|^2}{dR} \quad (2.13)$$

where  $m_e$  is the mass of the electron,  $M$  is reduced mass of the  $Rb-Xe$  complex,  $R$  is the internuclear separation,  $G$  is a parameter that depends on the spin orbit interaction of  $Xe$ , and  $\phi_1$  is the unperturbed electron wave function. This relation indicates that Cesium  $Cs$  could potentially couple better to  $Xe$  because of its larger mass and size.

### 2.3.2 Wall Collisions and Field Inhomogeneities

Additional relaxation mechanisms include collisions with the cell wall and magnetic field inhomogeneities. Wall collisions result in depolarization because the  $Rb$  atoms actually stick to the walls long enough to interact with the wall atoms. When the  $Rb$  atom is in contact with the wall, it is thought to bounce around thermally to different potential well sites on the wall. This behavior of the  $Rb$  atom can be modelled as a weakly perturbing fluctuating field as seen by the  $Rb$  atom [19].

When the magnetic resonance condition is far from being met, the spin relaxation due to the longitudinal component of static magnetic field homogeneities dominates over the transverse component [9]. The transverse component of field inhomogeneities become important only near the magnetic resonance condition. However, the  $Rb$  atoms are not being perturbed by any spin flip process, NMR or ESR (Electron Spin Resonance). Therefore, if  $D$  is the diffusion constant of  $Rb$ , then the relaxation is

given as:

$$\frac{1}{T_{long}} \approx D \frac{|\vec{\nabla} B_x|^2 + |\vec{\nabla} B_y|^2}{B_z^2} \quad (2.14)$$

## 2.4 Spin Exchange

### 2.4.1 Polarization Transfer

Spin exchange between *Rb* and *Xe* is a process that has a small probability to result in the exchange of the electron spin state of *Rb* with the nuclear spin state of *Xe*.

The interaction potential between *Rb* and *Xe* is given as:

$$V_{Rb-Xe} = \gamma(R) \vec{N} \bullet \vec{S} + \alpha(R) \vec{K} \bullet \vec{S} \quad (2.15)$$

The first term, which is discussed in the previous section, reflects the loss of the *Rb* electron spin angular momentum to the rotational angular momentum of the *Rb* and *Xe* atoms rotating about each other. The second term is a Fermi-contact hyperfine interaction that causes the spin exchange. A theoretical model for the spin exchange between a *Rb* and *Xe* atom developed by Herman [21] yields:

$$\alpha(R) = \frac{16\pi}{3} \frac{\mu_B \mu_K}{K} \eta^2 |\phi_1(R)|^2 \quad (2.16)$$

where  $\mu_B$  is the Bohr magneton,  $\mu_K$  is the nuclear magneton,  $K$  is the nuclear spin,  $\eta$  is a parameter that depends on the spin orbit interaction of *Xe*, and  $\phi_1$  is the unperturbed electron wave function. The parameter  $\frac{1}{x^2}$ , where  $x = \frac{\gamma N}{\alpha}$ , gives a measure of the efficiency of the spin exchange. For *Rb-Xe* about 10% of the interactions result in a successful spin exchange [10].

The spin exchange from *Rb* to *Xe* can occur in one of two ways. (1) The atoms

can simply undergo binary collisions:



(2) A three body van der Waals molecule can be formed for a short time [46]:



At high pressures the third body in the van der Waals molecule is typically another  $Xe$  atom, while at low pressures it is  $N_2$ . The spin exchange rate is given as [10]:

$$\gamma_{SE} = [Rb] \left( \langle v\sigma \rangle_{Rb-Xe} + \frac{\gamma_M \zeta}{[Xe]} \right) \quad (2.17)$$

For binary collision spin exchange, the rate is dependant only on the  $Rb$  concentration and the velocity averaged spin exchange cross section. On the other hand, the three body spin exchange rate is dependant on the constant  $\gamma_M$ , a parameter  $\zeta$  which depends on the nuclear spins & abundances of  $Rb$ , and inversely to the  $Xe$  concentration. This indicates that at high pressures, the dominant mechanism of spin exchange is binary collision. The pumping time for  $Rb$  is milliseconds, which is orders of magnitude less than  $Xe$  pumping time. Therefore  $\langle P_{Rb} \rangle$  can be thought of having achieved its steady state value. The time evolution of  $Xe$  polarization is given as:

$$P_{Xe}(t) = \frac{\gamma_{SE}}{\gamma_{SE} + \frac{1}{XeT_1}} \langle P_{Rb} \rangle \left( 1 - \exp^{-\left(\gamma_{SE} + \frac{1}{XeT_1}\right)t} \right) \quad (2.18)$$

where  $\frac{1}{XeT_1}$  is the relaxation rate of  $Xe$ .

### 2.4.2 Frequency Shift

An interesting consequence of spin exchange is a small frequency shift in the Rb absorption lines. This added with the Zeeman frequency shift due the classical magnetic field produced by the bulk magnetization of the polarized  $^{129}\text{Xe}$  yields (in the low field limit):

$$\Delta\nu = \frac{8\pi}{3} \frac{1}{h} \frac{g\mu_B}{2I+1} \kappa_0 \mu_{Xe} [Xe] P_{Xe} \quad (2.19)$$

where  $\kappa_0$  is determined experimentally. Taking advantage of this shift provides for a method to accurately measure the polarization of  $Xe$ . A detailed analysis of this process can be found in Romalis et al. [32].

## 2.5 Spin Relaxation of $Xe$

The relaxation of  $Xe$  polarization has a few different sources. The most obvious and dominant mechanism is  $Xe$  atom-wall collisions which causes relaxation by the same mechanism described for  $Rb$ -wall relaxation (see 2.3.2). The relaxation time due to this site to site motion is dependant on the sticking time of the  $Xe$  atom, the holding field that the atom is in, and the correlation time of the fluctuations. The correlation time is the bandwidth of the randomly fluctuating field [25].  $Xe$  wall relaxation, however, is more troublesome because  $Xe$  has a large electron cloud. This make it more polarizable than  $Rb$  and therefore more prone to stick to the cell walls. Thus  $Xe$  can also loose its polarization through spin exchange and spin rotation interactions with wall atoms as well. A secondary and ultimately limiting mechanism is the spin rotation interaction between two  $Xe$  atoms. The relaxation rate for this process is given by:

$$\frac{1}{T_{Xe-Xe}} = [Xe] \langle v\sigma \rangle_{Xe-Xe} \quad (2.20)$$

Interestingly enough, the dominant relaxation mechanism for  $^{131}\text{Xe}$  is the electric quadrupole interaction that occurs because the nuclear spin of  $^{131}\text{Xe}$  is  $\frac{3}{2}$  and not  $\frac{1}{2}$  [40]. The relaxation time of  $^{131}\text{Xe}$  is 4 orders of magnitude shorter than that of  $^{129}\text{Xe}$  which renders the polarization of  $^{131}\text{Xe}$  useless.

Far from resonance, the longitudinal component of the field inhomogeneities dominates and the relaxation rate is identical to the result quoted for  $Rb$  with  $D$  now being the diffusion constant of  $Xe$ . Near or at the magnetic resonance condition, the relaxation rate is dominated by transverse field oscillations (at high gas pressures) [9]:

$$\frac{1}{T_{trans}} \approx D \left| \vec{\nabla} B_z \right|^2 \quad (2.21)$$

This behavior is relevant only for  $^{129}\text{Xe}$  spins when polarization levels are being measured. Finally, any paramagnetic species in the cell greatly adds to the relaxation rate through magnetic dipole interactions [31]. Therefore, great care needs to be taken to limit the amount of paramagnetic contamination in the cell.

## Chapter 3

### System Design & Function

#### 3.1 Overview

This chapter will describe in detail the design, function, and performance of all of the system components. (1) A discussion of the materials used is given. Care is taken to avoid the use of highly paramagnetic materials for the storage and transport of the polarized gas. (2) The cell design is motivated and the cell preparation is described. (3) A gas system is built for the characterization & removal of contaminants from the cell as well as for filling the cell. Two main types of delivery mechanisms are used. One is the direct delivery of the sample to the probe via tubing. The other and more advantageous is the delivery of a frozen  $Xe$  sample. (4) A description and performance of these two mechanisms is presented.

#### 3.2 Materials Considerations

Components that come into direct contact with the polarized sample, or wet components, must not be strongly paramagnetic nor ferromagnetic. These materials cause relaxation in the sample through magnetic dipole interactions. Magnetic susceptibilities of relevant materials are listed in Tab. 3.1. Therefore, wet component materials are limited to glass, Teflon, Viton, brass, and Aluminum ( $Al$ ). Pyrex glass is chosen because of its relative ease to work with in terms of glassblowing. However, it must be prepared appropriately to minimize contamination & wall re-

<b>Name</b>	<b>Source</b>	<b>Formula</b>	<b>Type</b>	$\chi_M$
Iron	Stainless Steel	$Fe$	Ferromagnetic	-
Chromium	Stainless Steel	$Cr$	Paramagnetic	+180
Chromium Oxide	Stainless Steel	$Cr_2O_3$	Paramagnetic	+1960
Copper	Brass	$Cu$	Diamagnetic	-5.46
Copper Oxide	Brass	$CuO$	Paramagnetic	+259.6
Zinc	Brass	$Zn$	Diamagnetic	-11.4
Zinc Oxide	Brass	$ZnO$	Diamagnetic	-46.0
Aluminum	Aluminum	$Al$	Paramagnetic	+16.5
Aluminum Oxide	Aluminum	$Al_2O_3$	Diamagnetic	-37.0
Boron Oxide	Pyrex	$B_2O_3$	Diamagnetic	-39.0
Silicon Oxide	Pyrex	$SiO_2$	Diamagnetic	-29.6
Rubidium Oxide	$Rb + O_2 \rightarrow RbO_2$	$RbO_2$	Paramagnetic	+1527

Table 3.1: Magnetic Susceptibilities in cgs units of inverse megamol

laxation. These procedures are discussed later on in this chapter. Teflon is a class of polyfluorocarbon resins basically composed of long chains of Carbon atoms surrounded by Fluorine atoms in a helical pattern. It is, for the most part, chemically inactive because the Fluorine atoms are tightly bound to the Carbon atoms. Since Fluorine is the most electronegative atom, it strongly keeps its electrons to itself, which means that contaminants will have difficulty sticking to it. PTFE and PFA are the two varieties of Teflon used in the cell and delivery system. Viton is a polyfluoroelastomer commonly used to make O-rings. It has a similar chemical make up to that of Teflon with the added property that it is able to retain its shape after deformation in temperatures up to 200 °C.

Most vacuum components and fittings are made of stainless steel because of its strength and low outgassing properties. However, it cannot be used on wet parts because it is composed mainly of Iron (ferromagnetic) and Chromium (paramagnetic). Brass is a good alternative because it is an alloy made of Copper and Zinc which are both diamagnetic. However Copper Oxides, which accumulate over

time, are fairly paramagnetic. An alternative to brass is Aluminum which is slightly paramagnetic. One of the biggest advantages of Aluminum is that its oxides are diamagnetic. Coupled with its inexpensiveness and its availability in the form of Swagelok components, Aluminum makes an all around good material for the first iteration. However, there is still room for improvement because it is slightly paramagnetic and Aluminum Swagelok components are not as durable or rated as highly as their stainless steel and brass counterparts.

### 3.3 Cells

#### 3.3.1 Design

Glass cells are used to store the sample gas while it is being polarized. The cell is sketched in Fig. 3.1. The incident beam profile is typically a 2 in diameter circle. It is therefore beneficial for the cell to be cylindrical with roughly 2 in diameter windows sized to match the incident beam profile. This ensures that the photon flux is maximized through the cell, yielding higher optical pumping rates. Optical windows are used to maintain the optical quality of incident beam.

The length of the cell is chosen to minimize the surface area to volume ratio, which subsequently minimizes wall relaxation. A 2 in diameter and 2 in length, neglecting wall thickness, yields a volume of about 100 cc. Most imaging experiments typically require a nominal volume of 500 cc of sample at 1 atm room temperature. This corresponds to 5 atm at room temperature with this cell design. Although this requires that extra precautions need to be taken to prevent cell explosion, the high pressure is actually a benefit. It has been observed that high densities of noble gases broaden the *Rb* absorption line. This increases the photon absorption cross section which consequently increases the optical pumping rates and *Rb* polarizations.

#### 3.3.2 Components

The cells are meant to be refillable so that the same cells can be used for multiple studies. To that end, each cell has a glass valve and a small *Rb* reservoir. A

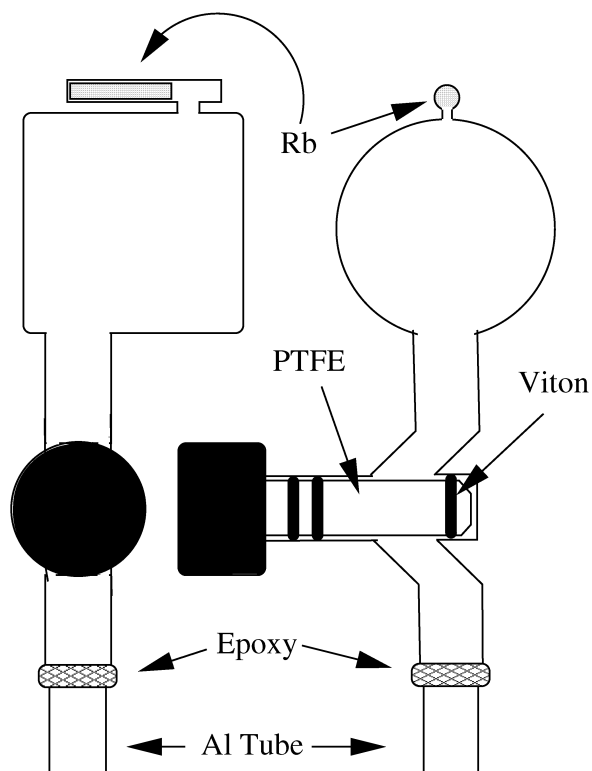


Figure 3.1: Glass Cell with Teflon Valve. The diameter and length of the cell are both 2”.

glass valve with a Teflon stem is used to seal the cell. It needs to be able to hold pressures up to 7.5 atm and maintain vacuum pressures down at least to  $10^{-6}$  torr. The high pressure limit is necessary because the cells are heated up to 175 °C to vaporize the *Rb*. The vacuum pressure limit is due to the fact that the cells are evacuated with the gas system to reduce the amount of residual contaminant gases such as  $O_2$ . The valve has been able to maintain pressures up to 120 psi = 8 atm = 6100 torr. Alternatively, its vacuum rating is quoted to be  $10^{-6}$  torr, but it has successfully managed vacuum pressures of an order of magnitude better. This type of valve will eventually have to be replaced for two reasons. During our polarization experiments, the O-ring would fail at temperatures below the quoted rating. Also, the Teflon stem sparks as the sample gas rushes through the opening. This is attributed to the fact that Teflon *is* reactive with alkali metals because of

their high electropositivity. Therefore chemical reaction between *Rb* vapor and the valve stem could be a source for relaxation. This was not known when the valve was selected.

The *Rb* reservoir can hold up to 1 gm of *Rb* which is more than enough for many polarization runs. A benefit to having the reservoir is that the excess *Rb* may react with some of the contaminants in cell not removed by the other processes. This also allows us to occasionally, only when necessary to replace the valve stem, expose the cell to air for short amounts of time  $\approx 10$  s. When exposed to air, the top layer of *Rb* reacts with the water and oxygen in the air forming a protective layer over the remaining *Rb* in the cell. *Rb* reacts with water to form  $H_2$  gas and *RbOH*, both of which are harmless to the polarization process. *Rb* reacts with  $O_2$  to form *RbO*<sub>2</sub>, which is highly paramagnetic. While this is not ideal, it is better to have the contaminants collected in the reservoir away from the main body of the cell as opposed to having those contaminants distributed homogeneously throughout the cell as a gas.

For the cell to be mounted to the gas and delivery systems, the glass cell needs to be coupled to metallic ports. Initially, ready made glass to metal seals were considered. However, when pressure tested, the seals would fracture between 3 to 4 atm. The alternate method, which proved far more successful, is to epoxy a piece of *Al* tubing onto the cell. The epoxy is known to outgas very little and is diamagnetic. These seals have been successfully tested to pressures of 11 atm and vacuum pressures down to  $10^{-8}$  torr.

### 3.3.3 Preparation

After the cell is made by attaching the windows and valve to the cell body, it is annealed at 500 °F to insure cell integrity. The annealing process also causes the cell to expand creating a cleaner and smoother inner cell wall that helps reduce wall relaxation. Before the cell is mounted to the gas system, it is cleaned with a basic rinse, an acidic rinse, and a deionized distilled water rinse. One noteworthy disadvantage of Pyrex is the fact that it tends to outgas impurities including water

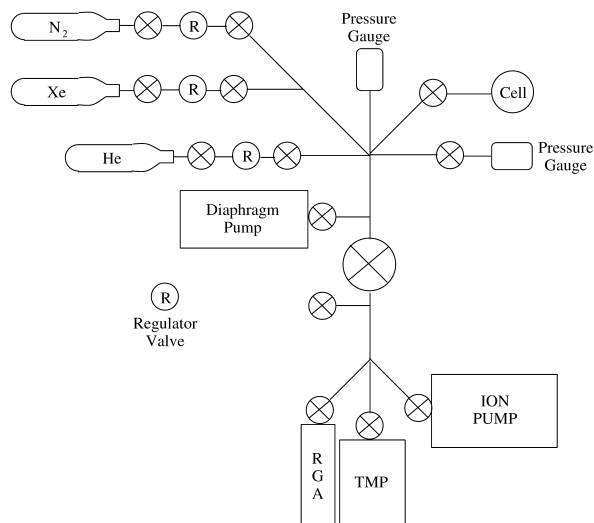


Figure 3.2: Gas System Schematic.

and  $O_2$  when heated. This is a major reason the cells are baked higher than typical run temperatures. The hope is that the contaminants stuck to the cell walls will be kicked off thermally and pumped away by the gas system.

The rinsed cell is dried in an oven and then glued to a piece of  $Al$  tubing. Next, it is mounted to gas system so that it can be pressure tested and then baked as described earlier. The effects of the bake will be described in the next section. After the bake, the  $Rb$  is liberated from the vacuum sealed ampoule and the ampoule is removed from the cell. For the polarization runs conducted so far, a nominal ratio of 4:1 natural abundance  $Xe$  (26.4%  $^{129}Xe$ ) to research grade (99.9999%)  $N_2$  is used to fill the cells.

### 3.4 Gas System

The gas system, Fig. 3.2, is vital to the cell preparation process. The three main uses of the system are (1) the removal of the contaminants from cell, (2) the establishment of the identity & quantity of the contaminants, and (3) the filling of the cell. A contaminant for our purposes is anything that is paramagnetic, that will cause relaxation by some other process, or that is unsafe in biological environments. The

gas system was assembled in a home made clean room. All the components came sealed and certified to semiconductor cleanliness standards. Roughly two months were dedicated to building and testing the gas system. Every joint was leak tested with *He*. Once the system was verified to be leak tight to vacuum pressures of  $10^{-10}$  torr, it was baked multiple times for days to remove contaminants from the system walls. Three different pumps are used evacuate the system. Because cell samples will eventually be entering biological environments, it is important for the system to remain as clean as possible. Therefore, none of the gas system components should introduce any new contaminants.

### 3.4.1 Contamination Removal

Contaminants are removed by three different pumps coupled to the system. These pumps work by different mechanisms and over slightly overlapping ranges. A diaphragm pump is a mechanical oil less pump that brings the pressure down from  $10^3$  torr to 1 torr. The turbomolecular pump or TMP brings the pressure down from 1 torr into the range  $10^{-4}$  to  $10^{-8}$  torr. It has a series of angled blades that spin at 1500 Hz which trap atoms and molecules individually and force them down and into an adjacent diaphragm pump. The ion pump brings the pressure down from as high as  $10^{-4}$  torr into the range  $10^{-6}$  to  $10^{-10}$ . It ionizes the atoms and removes them by accelerating them towards positively and negatively charged grids. These grids eventually become coated and need to be replaced once every five years. These pumps were chosen specifically because they are efficient at removing  $O_2$  &  $H_2O$  and they do not introduce contaminants back into the cell.

### 3.4.2 Contamination Characterization

A residual gas analyzer or RGA is used to identify and quantify the contaminants when vacuum pressures are sufficiently low enough ( $10^{-4}$  torr). Residual gas atoms and molecules are ionized with a filament. These ions travel to a portion of the RGA where an electrical quadrupole has been setup. The ions oscillate between the oppositely charged poles of the quadrupole with a characteristic frequency which

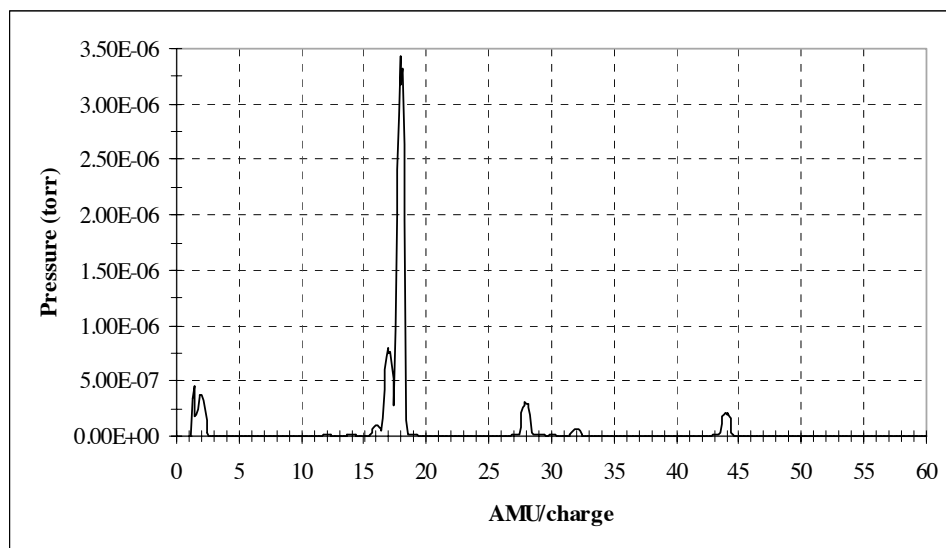


Figure 3.3: RGA Scan Before Bake. The peaks are (in order of size) 18,17-Water, 1-Hydrogen, 28-Nitrogen, 44-Carbon Dioxide, and 32-Oxygen

is dependant on its mass to charge ratio. Electrodes measure the frequency of the oscillations and a computer interfaced to the controller records the data.

RGA scans are taken before, during, and after the bake. Water dominates the prebake scan Fig. 3.3. The bake, which typically occurs at 175 °C, initially increases the system pressure by an order of magnitude. This is because a vast quantity (relative to the vacuum pressure) of water is being baked off the cell walls faster than the pumps can remove it. The vacuum pressure reaches a peak value when the partial pressure of the outgased substances in the solid and gas phase come into equilibrium at the higher temperature. The vacuum pressure stays at this point until the quantities of the outgased substances is greatly reduced. Afterwards the system pressure drops slowly to it's final equilibrium value. Water, nitrogen, and hydrogen are the main peaks after the bake Fig. 3.4, while the system pressure is by about an order of magnitude less.

Care must be taken when interpreting RGA data because these pressures represent measurements made far from the cell and therefore may differ from actual cell values in magnitude and relative proportions. This 'lag' effect can be gauged to

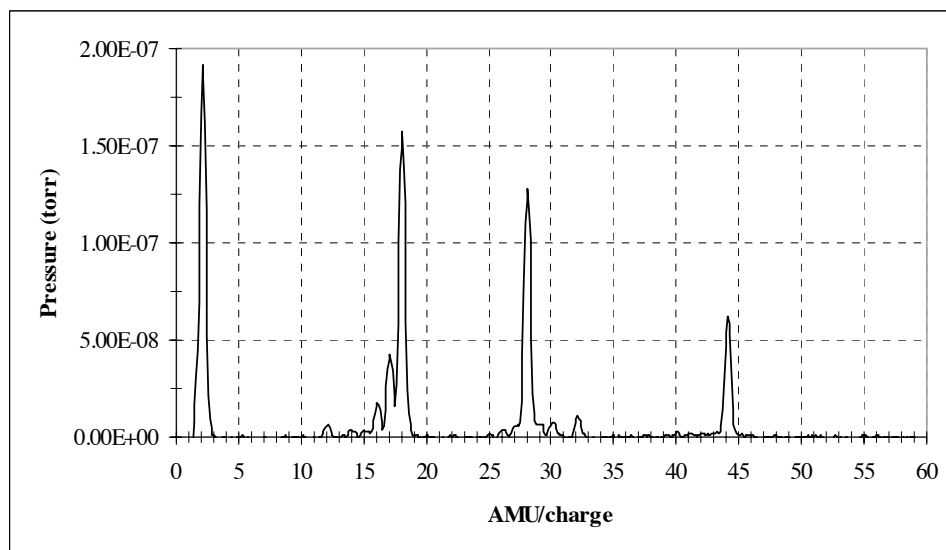


Figure 3.4: RGA Scan After Bake. The peaks are (in order of size) 1-Hydrogen, 18,17,16-Water, 28-Nitrogen, 44-Carbon Dioxide, and 32-Oxygen.

some degree by comparing the total pressure reading near the cell with one taken near the TMP. Typically differences are about an order of magnitude. This discrepancy comes from the fact that components on the system with smaller cross sectional areas are pumped slower. Equilibrium between all parts of the system can be achieved after a long time (about 3 days).

### 3.4.3 Cell Filling

Since the gas system is used to fill as well as to evacuate, it is important to isolate the vacuum sensitive components from high pressure. A specially designed valve, which has the unique property of being able to contain both high pressures ( $> 200$  psi) and high vacuums ( $\approx 10^{-10}$  torr), was ordered from Swagelok. This part of the gas system was carefully designed to minimize waste. As a result, roughly 1 mol of gas is lost for every 2 mols of gas stored in the cell. A cryofilling method, which will reduce waste to negligible amounts, will be developed as a part of the long term plan. A vacuum gauge is located near the cell to measure the residual

gas levels before the fill. A pressure gauge is also located near the cell to measure the final cell fill pressure. Along with an adaptable port for the cell, there are three ports for the four possible fill gases: natural  $Xe$ , enriched  $Xe$  ( $\approx 80\%$ ),  $N_2$ , and  $^4He$ . Any mixture of three of the four gases can be created. My cells contain a 4:1 mixture of natural  $Xe$  to  $N_2$ . For comparison, other research groups typically use proportions of around 1:1:98 of enriched  $Xe$  to  $N_2$  to  $^4He$  [3]. They use a high density of  $^4He$  to pressure broaden  $Rb$  absorption line. It should be noted that enriched  $Xe$  costs roughly two orders of magnitude more than natural  $Xe$ . It is not clear what the most effective and cost efficient mixture is, therefore gas mixture studies will become a part of the long term research plan.

## 3.5 Optical System

### 3.5.1 Overview

The cell, which is mounted in an oven, is placed in the beam line at the center of large Helmholtz coils. A regulator or a feedback temperature controller is used to bring the cell to the appropriate temperature. The  $Rb$  vapor pressure is given by the following equation over the range  $313\text{ K} \leq T \leq 550\text{ K}$  [8]:

$$\log\left(\frac{P}{1\text{ Pa}}\right) = 9.318 - \frac{4040\text{ K}}{T} \quad (3.1)$$

The temperature is adjusted to match the  $Rb$  absorption cross section with the incident laser photon flux such that the cell contains no regions of unpolarized  $Rb$ . The light from the laser is tuned to 794.8 nm, the D1 line of  $Rb$ . First, the beam travels through a lens to produce a 2" collimated beam. A polarizing cube splits the incident beam into two beams having orthogonal linear polarizations relative to each other Fig. 3.5. The beams, which are redirected to the cell by mirrors, are circularly polarized by quarter waveplates. The quality of circular polarization is calculated by measuring by the intensities of left and right circular polarization:

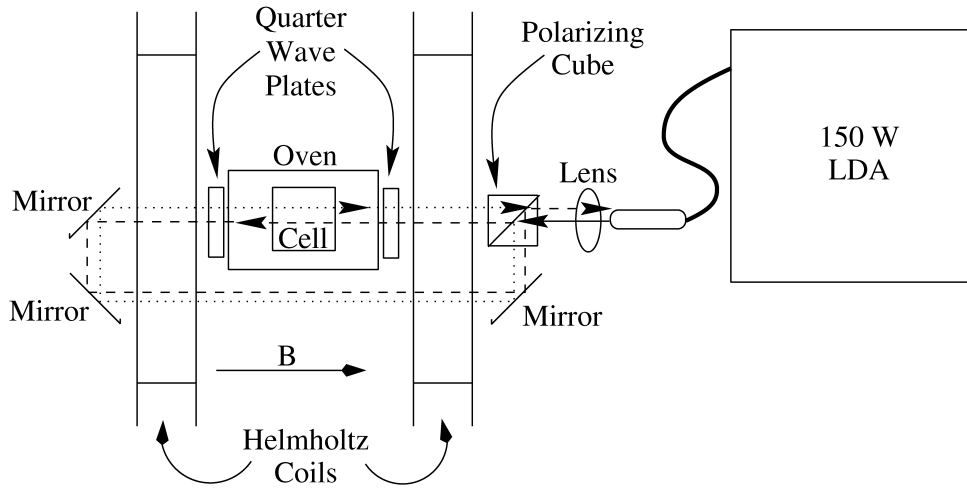


Figure 3.5: Optical Setup. The cell is being pumped from both windows using the 150 W LDA.

$$P_{light} = \left( \frac{I_+ - I_-}{I_+ + I_-} \right) \quad (3.2)$$

Typical values for  $P_{light}$  are about 0.99.

### 3.5.2 Pressure Broadening of *Rb* Absorption Lines

As mentioned before, large densities of buffer gas broaden the *Rb* absorption line. This broadening is thought to arise from the van der Waal interaction between the *Xe* and the *Rb* atoms. Romalis et al. have experimentally found the pressure broadening to be linear with pressure (more or less temperature independent) and given as  $18.9 \pm 0.5$  GHz/amagat for *Xe* and  $17.8 \pm 0.5$  GHz/amagat for  $N_2$  [30]. An amagat is the number density of a gas at STP,  $2.46148 \times 10^{19} \text{ cm}^{-3}$ . For a 100cc 5 atm cell with a 4 to 1 *Xe* to  $N_2$  gas mixture, the pressure broadened line width is roughly 95 GHz. This corresponds to an absorption line width of roughly 0.20 nm. In the next section, this line width is compared to the incident beam line width. Incidentally, pressure broadening is an on going project in our lab that was

initiated with Emma Goldberg in 1999.

### 3.5.3 Laser Systems

Three different laser systems are used. Two of these systems are Laser Diode Arrays (LDA). Two 30 W LDAs were used initially for the portable system. A more powerful 150 W LDA is currently being adapted for the portable setup. LDAs are cheap ( $\approx$ \$150 per W), small, put out a lot of power, and they have an emission line width of roughly 2.5 nm (full width half maximum) Fig. 3.6. The broad linewidth is both a benefit and a disadvantage. The advantage is that the laser will be emitting wavelengths that cover the absorption line width even if the central laser frequencies happen to drift. The downside is that the power usage is very inefficient since the largest absorption line width is 0.20 nm. These lasers are tunable over a 10 nm range by adjusting the diode current and temperature. A spectrum analyzer has to be used to tune the beam to the correct wavelength.

The head for the 30 W lasers is actually a bundle of about 20 smaller optical fibers, see Fig. 3.7. The head of the 150 W LDA is actually a bundle of 10 independent heads which in turn are each a bundle of about 20 optical fibers. By independent I mean that each subhead has a separate control. The discreteness of the heads results in a nonuniform beam profile, which in turn results in uneven polarization in the cell. To maximize polarization, it is essential that the beam profile is relatively uniform. This problem is remedied effectively by using the lens to blur the spatial profile of the beam as well as to collimate the beam. However, this is not entirely the case for the 150 W laser. The power from all 10 heads is higher than the allowable power ratings for most of the optics in our lab. Therefore, only four of the heads are turned on ( $\approx$ 60 W), but this results in a much more discrete & nonuniform beam profile. Once again it is remedied, but not as effectively, with a lens. A novel technique, that is being used to address this problem, is pumping on the cell from both sides. The hope is that this will result in a more uniform distribution of the beam in the cell.

The third system is an array of four 5 W Ti:Sapphire lasers. For the sapphire

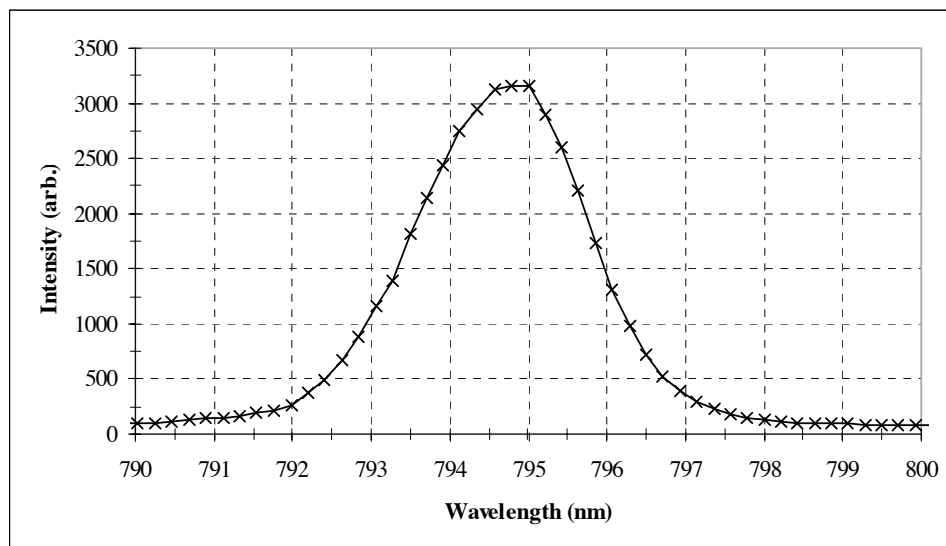


Figure 3.6: LDA Emission Spectrum.

crystal to be lased, it must be pumped on by a 20 W Ar<sup>+</sup> laser. The set is therefore much bigger and more expensive ( $\approx$  \$18,000 per W) than a single LDA. At first glance, it seems that this laser system puts out less power. However, the emission line width is  $\approx$ 0.10 nm. This makes practically all of the output power usable. The downside in this case is that if the laser for some reason drifts, the almost all of the output power is lost. These lasers can be tuned over a range of 100 nm by adjusting the inner cavity path length of the Ti:Sapphire. Since the emission line width is so small, one can actually see the extinction of the beam in the cell (using IR viewers of course). This is in fact the method used to tune the lasers to absorption. The beam profile is roughly Gaussian coming out of the laser, but by the time it reaches the cell, it is more or less uniform.

### 3.5.4 Coils

Two sets of coils powered by high voltage supplies are used to provide the holding field for the optical pumping. If the coil separation is chosen to be equal to the coil radius, then fairly uniform magnetic fields are produced at the middle/center

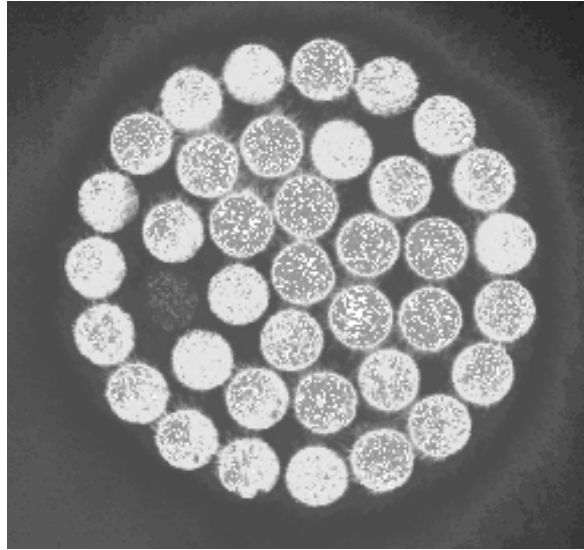


Figure 3.7: Magnified Beam Profile. This is a typical beam profile of a 30 W LDA. Note the spatial distribution of photons in the beam.

region of the coils. The coils used in our lab are the 75 cm radius coils used at SLAC during the spin structure experiments. These coils create the holding field for both optical pumping and for AFP. The cell sits about 50 cm off the holding field axis. This does not harm the polarization much for two reasons. First, the cell diameter of 5 cm is much smaller than the coil radius. Second, the transverse magnetic field gradients become a dominant factor in relaxation only when AFP is being performed. In this case, the cell is connected to a probe, where the AFP occurs, which is at center of the coils. A second, portable set of coils of radius 30 cm were constructed. The cell length to coil radius ratio in this case is larger, but the cell sits in the center of these coils. The longitudinal field gradients caused by the big magnet are negligible, if the coils are sitting at least 10 ft away.

### 3.6 Delivery Mechanisms

The delivery mechanism is the most difficult component to design because of all the parameters to consider. (1) The mechanism has to be made of nonparamagnetic

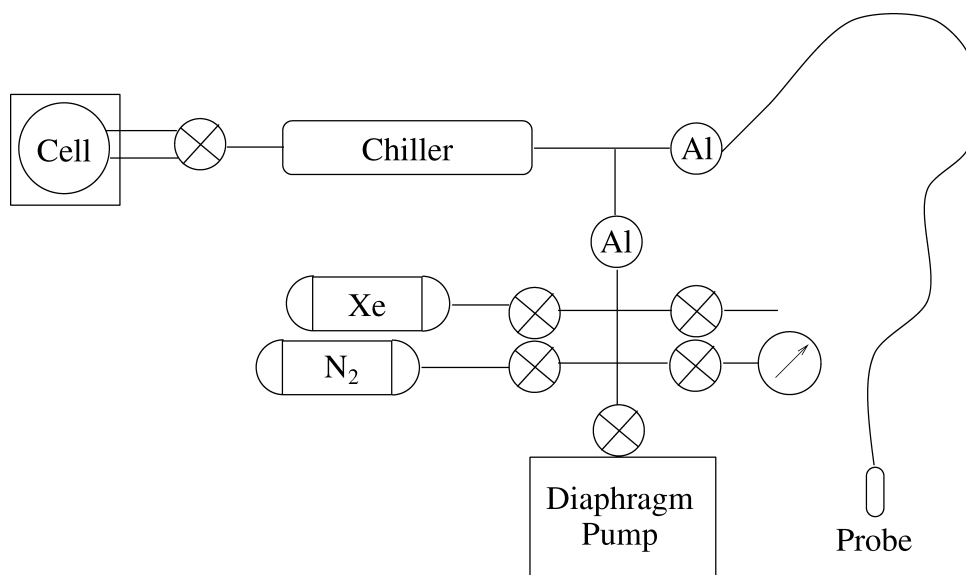


Figure 3.8: Delivery Line Schematic. The cell is sitting in the coils and the probe is inserted into the pick up coils for measurement.

materials. (2) It must remain contaminant free during the delivery process. (3) The mechanism must have a way to remove the *Rb*, because the sample will eventually be delivered to a biological environment. (4) It needs to be resistant to the fact that the 11.7 T imaging magnet introduces field gradients along the delivery path that require the spins to rotate by at least  $90^\circ$ . (5) The mechanism must be efficient in that it minimizes waste caused by delivery. The initial designs involved the direct delivery of the gaseous sample from the cell to the probe via tubing. This design was found to be cumbersome and faulty. The current design involves the freezing of *Xe* in  $\text{LN}_2$ . It has been shown [15] that this technique greatly reduces the relaxation rates. Frozen *Xe* is the technique being developed at the time of writing of this document.

### 3.6.1 Gaseous Delivery

The delivery line approach has gone through a few generations, but the general idea is depicted in Fig. 3.8. The tubing for the main line has been designed using both

PFA and Aluminum, each having desirable and undesirable properties. PFA tubing is very flexible and therefore easy to use. *Al* tubing is pliable, but is still very stiff. There is no way to thoroughly clean the inner walls of PFA tubing. The *Al* line, on the other hand, is baked and evacuated with the gas system, presumably yielding a cleaner environment. Note however, that the PFA starts cleaner than the *Al*. Ideal Swagelok connections occur between two identical materials. The main line is connected to *Al* valves at two points. *Al* tubing has the advantage that the seals made at those points are guaranteed to  $10^{-8}$  torr which is better than PFA/*Al* seals.

The line is attached to a probe that has dimensions that maximizes the filling factor in the pickup coils. While the sample is being polarized, the probe and line are overpressured with a buffer gas, preferably  $N_2$ . If there is a leak on the line, then  $N_2$  will leak out and  $O_2$  will be impeded from leaking in. Before each fill, the line is pumped out with a diaphragm pump. Because of these procedures, the system contains a T off the main line with ports for a pump and a gas tank. There is an *Al* valve between the T and the main line that keeps the polarized gas away from the stainless steel components of the pump and purge ports. It should be noted that the cell volume and line volume are roughly equal, so each fill reduces the  $Xe$  density by a factor of two. A chiller filled with cold water surrounds an *Al* tube leading away from the cell. *Rb* melts at  $40\text{ }^\circ\text{C}$ , so running the chiller at  $10\text{ }^\circ\text{C}$  is adequate to freeze out the *Rb*. Studies will have to be done to determine the best mechanism to remove *Rb* before the sample is delivered.

Perhaps the largest unknown to consider is the magnetic field gradient between the cell and the probe. At the cell, a field of  $\approx 80$  gauss is pointing towards the magnet. At the probe where the sample is measured, a field of 11.7 T is pointing towards the ceiling. The hope is that the spins will follow the field adiabatically. An effort is made to the shape and bend the line to follow the field. Studies regarding the field gradients will have to be performed to determine the feasibility of this delivery technique.

### 3.6.2 Frozen Xe Delivery

Gatzke et al. reported that the relaxation times of frozen polarized  $^{129}\text{Xe}$  held at a field of  $\geq 100$  gauss are on the order of hours. The mechanism of relaxation from 20 K to 120 K in high magnetic fields ( $> 500$  gauss) is dominated by the nuclear spin flip Raman scattering of phonons [13]. The interaction term is given as

$$V_{fXe-Xe} = a \vec{K} \bullet \vec{N} \quad (3.3)$$

This is again a spin rotation interaction between two adjacent  $Xe$  atoms in the solid. Phonons in the crystal are absorbed and emitted by neighboring atoms causing spin flips. When the temperature is below 20 K, the relaxation is dominated by cross relaxation with  $^{131}\text{Xe}$ . Relaxation times are relatively field independent above 500 gauss, but are dependent on temperature exponentially. Experimentally determined, the relaxation time at 77 K above 500 gauss is on the order of 3 hrs. At 100 gauss and 77 K, the relaxation time is found to be about an hour. A set of two 4 cm diameter coils with about 160 turns per cm can be powered with four 1.5 V AA batteries for about 2 hrs. This setup provides a holding field for the frozen  $Xe$  on a time scale much longer than needed to run the experiment. The sample is frozen in a cold finger made of glass that is immersed in  $\text{LN}_2$ . Once the sample has been collected, the cold finger can be detached and physically delivered to the probe. When the cold finger is removed from the  $\text{LN}_2$ , the frozen  $Xe$  sublimates into the probe. This system is better because (1) delivery relaxation losses are minimized and (2) all of the sample is transferred to the probe. The  $Rb$  will plate out and remain in the 77 K cold finger. It is clear why this method shows much promise; unfortunately, it is not clear how the sample will react to the field gradients near the magnet.

## Chapter 4

# Signal Measurement & Data Analysis

### 4.1 Overview

Nuclear Magnetic Resonance (NMR) refers to a whole class of techniques used to measure the polarization of a sample. They are all based on the idea that some mechanism causes the individual spins of the sample to rotate off the holding field axis, thereby causing an *EMF* in pickup coils proportional to the level of polarization. A basic quantum mechanical analysis is presented in Appendix B. The technique used in our lab is called Adiabatic Fast Passage. In theory this technique should result in no loss to the polarization of the sample. One way to calculate the polarization in the sample is to model the coil and electronics and find an analytic relationship between the signal and the polarization. This is difficult because there are predictable but high sources of errors and unpredictable sources of error. Therefore, a measurement of a known proton thermal polarization serves as the calibration for AFP. Pulsed NMR is the method used in the Fraser MRI Lab to obtain an MR spectra. Unfortunately, pulsed NMR causes an irrevocable loss of polarization. The signals obtained by this method are calibrated using a *Xe* thermal signal. Another measurement technique currently being developed in our lab takes advantage of the *Rb* Zeeman frequency shift mentioned before. This technique as well as proton calibration were both developed at Princeton for the spin structure experiments at SLAC.

## 4.2 NMR AFP

### 4.2.1 Overview

The technique of Adiabatic Fast Passage is used to measure the polarization of a sample of  $^{129}\text{Xe}$  without incurring any substantial loss of polarization. In AFP, an oscillating field is applied perpendicular to the holding field that the sample is in. The spins of the sample follow the  $B$ -field which is being swept through the magnetic resonance value. The sweep has to occur fast enough to insure that little polarization is lost at resonance due to the oscillating field, but slow enough for the spins to follow the field.

### 4.2.2 Description

Consider a situation where a collection of spins are collected in a large holding field  $\vec{B}(t)$  and an rotating orthogonal field  $\vec{B}_1(t)$ . In the lab frame,  $\hat{x}_{rot}$  is a unit vector that is co-rotating with the spins with frequency  $\omega_0$ . Therefore the effective field felt by the spin is (see Appendix B.):

$$\vec{B}_{eff}(t) = \left( B(t) - \frac{\omega_0}{\gamma} \right) \hat{z} + B_1 \hat{x}_{rot} \quad (4.1)$$

Note that the bulk magnetization of the sample  $\vec{M}$  always points in the direction of  $\vec{B}_{eff}$ , while the individual spins precess about  $\vec{B}_{eff}$ . The spins flip over during the sweep, therefore, it is customary to sweep the field through resonance twice thereby flipping the spins twice. When  $B(t)$  is far from  $B_0 = \omega_0/\gamma$ ,  $\vec{M}$  has a small component transverse to the holding field. As  $B(t)$  is swept through resonance at  $B_0 = \omega_0/\gamma$ ,  $\vec{M}$  is pointing mainly transverse to the holding field. Refer to Fig. 4.1 for a graphical description of this process.  $\vec{M}$  produces an *EMF* in the pickup coils which is proportional to the polarization and the resonant frequency. The line shape of the signal is given by (see Appendix B):

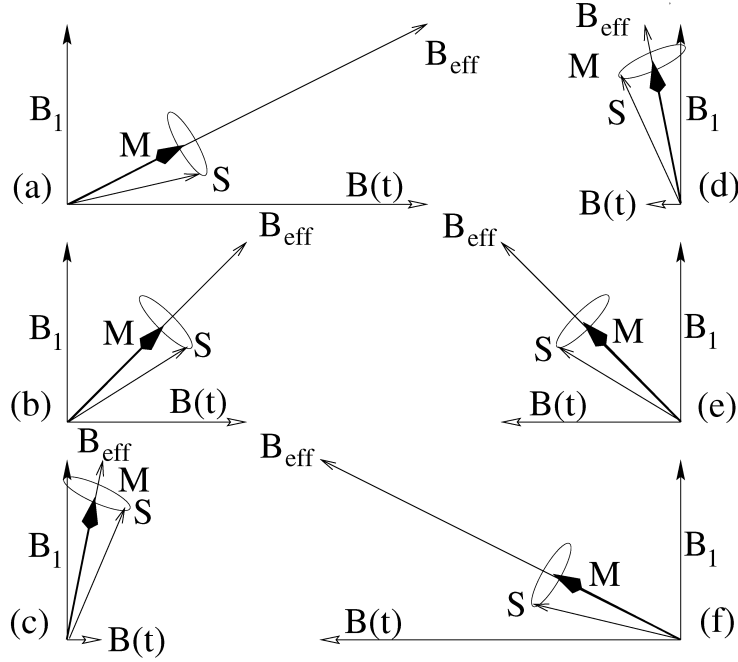


Figure 4.1: AFP Sweep. Time increases alphabetically. The spin is precessing about the effective B field.

$$S(t) \propto \omega_0 M \frac{B_1}{\sqrt{(B(t) - B_0)^2 + B_1^2}} \quad (4.2)$$

### 4.2.3 AFP Conditions

The holding field must be swept slow enough to allow the spins to follow adiabatically. The precession of the spin about the field can be thought of as the ‘force’ that keeps it pointing along the field. If the spins are precessing fast enough about  $\vec{B}_{eff}$ , then it will follow  $\vec{B}_{eff}$  adiabatically. Therefore, the rate of the sweep is most important during resonance when  $\vec{B}_{eff}$  has it’s lowest value. Thus, the first of two conditions required for AFP is:

$$\frac{1}{B_1} \left| \frac{dB(t)}{dt} \right| \ll \gamma B_1 \quad (4.3)$$

The other condition is mentioned when  $Xe$  relaxation mechanisms are discussed. It has been found that near resonance, small transverse field oscillations cause relaxation with rates:

$$\frac{1}{T_{trans}} \approx D \left| \vec{\nabla} B_z \right|^2 \quad (4.4)$$

To insure that the AFP measurement does not cause a substantial loss of polarization, the holding field sweep rate should be much faster than the relaxation rate due to the small oscillating transverse fields. Putting it all together, the condition for AFP is:

$$D \frac{\left| \vec{\nabla} B_z \right|^2}{B_1^2} \ll \frac{1}{B_1} \left| \frac{dB(t)}{dt} \right| \ll \gamma B_1 \quad (4.5)$$

#### 4.2.4 Experimental Setup

A schematic of the apparatus is given in Fig. 4.2. The holding field  $B$  is created by a set of large Helmholtz coils. When a measurement is being taken, the field is swept with a function generator that outputs a triangular waveform to the high voltage power supply running the coils. The oscillating field  $B_1$  is created by a set of smaller coils in the center of the holding field. Another function generator outputs a sine wave at the radiofrequency (RF)  $\frac{\omega_0}{2\pi}$  that travels to the RF amp. The RF coils receive an amplified signal from the RF amp. A set of two pickup coils sit in the center of the Helmholtz coils. The induced signal travels from these coils through a preamp to the lock-in amp. Because the RF coils and the pickup coils cannot be made to be perfectly orthogonal, a background signal at the RF frequency is also induced in the pickup coils. A cancellation signal generated from

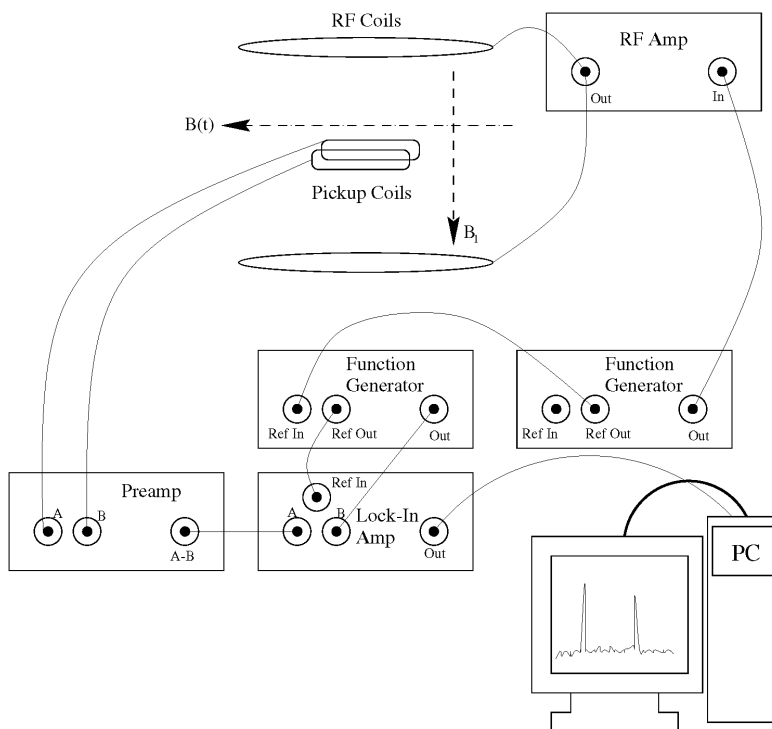


Figure 4.2: AFP Electronic Apparatus. The apparatus also includes a sweep generator (not pictured) that is connected to the coil creating the holding field.

another function generator is sent to the lock-in amp. The cancellation is done manually by adjusting the phase and amplitude of the cancellation signal which is also sent to the lock-in amp. Reference frequency signals are sent to the lock-in amp and the function generator creating the cancellation signal from the function generator driving the RF coils. The lock-in amp stores the sweep data in a buffer. A computer interfaced with the sweep generator and the lock-in amp controls the sweep electronics and stores the sweep data.

### 4.3 Pulsed NMR

Pulsed NMR is the technique used to measure the thermal and polarized signals in the Fraser MRI Lab. An RF pulse of frequency  $\nu$  and duration  $t_{RF}$  causes the bulk magnetization of the sample  $\vec{M}$  to tip by an angle  $\alpha$ . Typical tipping angles are

about  $10^\circ$ . A component of  $\vec{M}$  is rotated to a direction transverse to the holding field and induces a signal in the pickup coils:

$$S \propto \omega_0 M \sin(\alpha) \quad (4.6)$$

Correspondingly, the component of  $\vec{M}$  still aligned with the holding field is reduced by a factor  $\cos(\alpha)$ . After  $n$  pulses, the resulting magnetization is:

$$\vec{M}_n = M_0 \cos^n(\alpha) \exp\left(-\frac{nt_{RF}}{T_{Xe}}\right) \hat{z} \quad (4.7)$$

The transverse component of  $\vec{M}$  is lost very quickly, while the longitudinal component decays exponentially as a function of the relaxation rate of  $Xe$ . Generally the pulse parameters are set up in such a way that the relaxation losses to polarization are negligible to the measurement losses which simplifies the analysis.

## 4.4 Calibration

### 4.4.1 Thermal Water Proton Polarization

Signals produced by thermally polarized protons in water are measured as a calibration for AFP. The two largest obstacles to this technique are the very small polarization level achieved and the long relaxation time of the protons. The relaxation time in this case refers to the amount of time it takes for  $(1 - e^{-1}) \approx 63\%$  of the protons to return to thermal equilibrium in the field that it sees. The fact that very low levels of polarization are achieved is partially offset by the fact that densely populated liquid water is used. Still around 20 signals are still needed to be averaged to increase the SNR enough to get a useful peak.

The second obstacle is more difficult to resolve. As the field is swept, the thermal polarization of the protons is changing because the field is changing. The amount of time it takes the protons to reach the new equilibrium is on the order of

the sweep time. This means that not all of the protons have equilibrated by the time the field changes again. The results is a measurement of a polarization value lower than the predicted amount. Thus, the Bloch equations must used to model the time evolution of the proton spins during the sweep:

$$\begin{aligned}
\frac{dM_x}{dt} &= \gamma M_y (B - B_0) - \frac{(M_x - \chi B_1)}{T_2(B_1)} \\
\frac{dM_y}{dt} &= -\gamma M_x (B - B_0) + \gamma M_z B_1 - \frac{M_y}{T_2(B_1)} \\
\frac{dM_z}{dt} &= -\gamma M_y B_1 - \frac{(M_z - \chi B_1)}{T_1} \\
B &= B_0 + \alpha t
\end{aligned} \tag{4.8}$$

where  $M$  is the magnetization,  $T_1$  is the longitudinal relaxation time,  $T_2$  is the transverse relaxation time, and  $\chi$  is the magnetic susceptibility of the sample. Using simplifying assumptions and series expansion, one can derive an analytic solution to the line shape expected from protons. Detailed analysis of this problem can be found in Middleton [27] and Romalis [31]. The final result is a correction of about 5% or  $x \approx 0.95$ . To see what other factors need to be considered, it is necessary to follow the path of the signal from the coils to the computer.

The net magnetization that is being measured is:

$$M = \left( \frac{\gamma \hbar}{2} \right) \rho P \tag{4.9}$$

The density of the sample is  $\rho$ . The total number of spins located within the region between the coils is what contributes to the the overall magnetization measured. Neglecting diffusion effects, the cross sectional area of the probe transverse to the coil is proportional to the number of spins. If it is assumed that the probe is longer than the coils, then the total number of spins scales as  $R^2$  where  $R$  is the radius of the probe.

The signal induced in the pickup coils is given as:

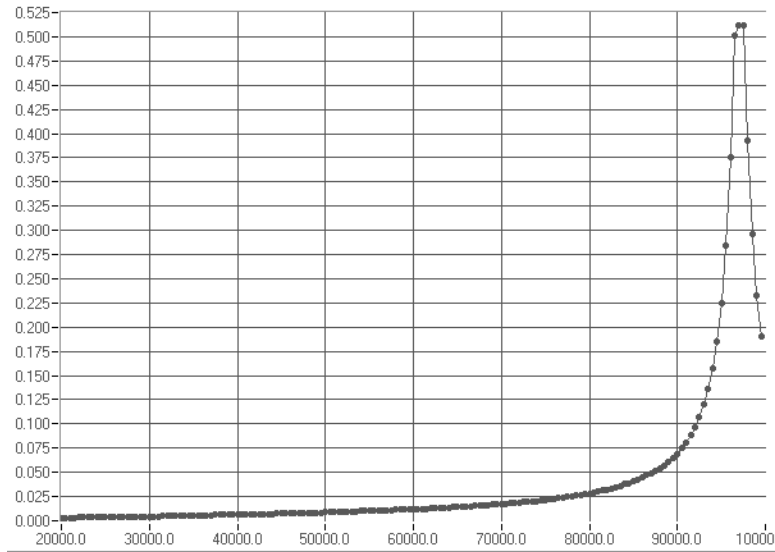


Figure 4.3: Q Curve of the Pickup Coils used for AFP. The x-axis is the frequency in Hz and the y-axis is the response in arb. units.

$$S \propto \omega_0 M A \quad (4.10)$$

$A$  is a parameter associated with the amount of area in the coils that feels the changing flux. This is a function of probe size and placement. Assuming that the probe is large enough to make errors in placement negligible, then  $A$  is proportional to the longitudinal cross sectional area of the probe. Since it is assumed that the length of the probe is longer than the length of the coils,  $A$  scales as  $R$ . The pickup coils are two heavily wrapped wires that are connected to a capacitor in parallel. The coils form an RLC circuit, therefore its response is a function of frequency  $Q(\omega)$ . By pulsing the coils at different frequencies and measuring the response, one can generate a plot of  $Q(\omega)$  called the Q curve. For the coils used in our lab, the Q curve is depicted in Fig. 4.3. Once the signal is produced in the coils, it is sent through a preamp that amplifies the signal by an amount  $G_{preamp}$ . The signal travels through a cable, experiencing some signal attenuation  $G_{loss}$ , to the lock-in

amp. The lock-in amp gains the signal by some amount  $G_{lockin}$  and is then stored by the computer. The computer records voltage vs. time. This signal can then be fit to a Lorentzian curve with a background and linear offset:

$$f(x) = \frac{c_0}{\sqrt{\left(\frac{x-c_1}{c_2}\right)^2 + 1}} + c_3 + c_4x \quad (4.11)$$

Once the  $Xe$  and water signals are fit, one can extract the peak size. The voltage peak extracted from the fit is related to the polarization by:

$$V = \left(\frac{\gamma\hbar}{2}\right) \rho P \omega_0 R^3 Q(\omega_0) G_{preamp} G_{loss} G_{lockin} k_{other} \quad (4.12)$$

A constant  $k_{other}$  is multiplied to account for other systematic gains and losses of the signal assumed to be independent of the sample and probe used. It is reasonable to assume that  $G_{loss}$  &  $G_{lockin}$  are independent of the sample and the probe used as well. Putting this all together for water protons yields:

$$V_{1H} = \left[ \gamma_{1H} \rho_{1H} \left( x \frac{\hbar\omega_{1H}}{2kT} \right) \omega_{1H} R_{1H}^3 Q(\omega_{1H}) G_{preamp}^{1H} \right] \cdot \left( \frac{\hbar}{2} G_{loss} G_{lockin} k_{other} \right) \quad (4.13)$$

Defining  $C$  as the scaling constant:

$$C = \left( \frac{\hbar}{2} G_{loss} G_{lockin} k_{other} \right) = V_{1H} \left[ \gamma_{1H} \rho_{1H} \left( x \frac{\hbar\omega_{1H}}{2kT} \right) \omega_{1H} R_{1H}^3 Q(\omega_{1H}) G_{preamp}^{1H} \right]^{-1} \quad (4.14)$$

Therefore, we have for  $^{129}Xe$ :

$$\begin{aligned}
P_{129Xe} &= [(C) \gamma_{129Xe} \rho_{129Xe} \omega_{129Xe} R_{129Xe}^3 Q(\omega_{129Xe}) G_{preamp^{129Xe}}]^{-1} V_{129Xe} \\
&= \left( \frac{V_{129Xe}}{V_{1H}} \right) \left( x \frac{\hbar \omega_{1H}}{2kT} \right) \left( \frac{\gamma_{1H}}{\gamma_{129Xe}} \right) \left( \frac{\rho_{1H}}{\rho_{129Xe}} \right) \\
&\cdot \left( \frac{\omega_{1H}}{\omega_{129Xe}} \right) \left( \frac{R_{1H}}{R_{129Xe}} \right)^3 \left( \frac{Q(\omega_{1H})}{Q(\omega_{129Xe})} \right) \left( \frac{G_{preamp^{1H}}}{G_{preamp^{129Xe}}} \right) \quad (4.15)
\end{aligned}$$

#### 4.4.2 Thermal Xenon Polarization

Signals produced thermally from  $^{129}\text{Xe}$  are measured to calibrate signals in the Fraser MRI Lab. Again, the same two problems persist as they did for the proton calibration. The density is very small, therefore maximal pressures are used and thousands of sweeps are taken. The relaxation time of  $^{129}\text{Xe}$  can be made much smaller than the pulse duration by adding  $\text{O}_2$  to the gas mixture. Therefore, the correction factor  $x$  is negligible. The signal induced in the pickup coils is given as:

$$S \propto \omega_0 M A \sin(\alpha) \quad (4.16)$$

A probe with similar dimensions is used in either case, so  $A$  factors out of the final equation. The MR frequency  $\omega_0$  is slightly different because thermal  $^{129}\text{Xe}$  is chemically shifted due to the presence of  $\text{O}_2$ , while the hyperpolarized sample is not. The coils can be tuned to be around  $\omega_0$  by adjusting the capacitor. This is parameterized once again by using the Q curve of the coil  $Q(\omega)$ . Once the signal is produced in the coils, the signal is sent through a series of electronics within the MRI machine. The overall signal amplification and attenuation will be designated by  $G_{tot}$ . The MRI machine records voltage vs. time. This signal can then be fit to a Lorentzian curve with a background and linear offset. Once the thermal and hyperpolarized  $^{129}\text{Xe}$  signals are fit, one can extract the peak size. The voltage peak extracted from the fit is related to the polarization by:

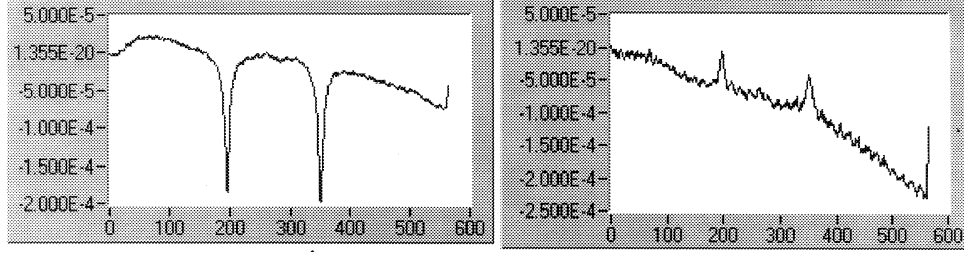


Figure 4.4: First AFP Signal. There are two peaks because the field is swept through resonance twice.

$$V_{th} = \left( \frac{\gamma \hbar}{2} \right) \rho_{th} P_{th} \omega_{th} Q(\omega_{th}) G_{tot} \sin(\alpha_{th}) \quad (4.17)$$

Defining  $C$  as the scaling constant:

$$C = \left( \frac{\gamma \hbar}{2} G_{tot} \right) = V_{th} [\rho_{th} P_{th} \omega_{th} Q(\omega_{th}) \sin(\alpha_{th})]^{-1} \quad (4.18)$$

Therefore, we have for  $^{129}\text{Xe}$ :

$$\begin{aligned} P_{^{129}\text{Xe}} &= [(C) \rho_{th} P_{th} \omega_{th} Q(\omega_{th})]^{-1} V_{^{129}\text{Xe}} \\ &= \sin^{-1}(\alpha_{^{129}\text{Xe}}) \left( \frac{V_{^{129}\text{Xe}}}{V_{th}} \right) \left( \frac{\hbar \omega_{th}}{2kT} \sin(\alpha_{th}) \right) \\ &\quad \cdot \left( \frac{\rho_{th}}{\rho_{^{129}\text{Xe}}} \right) \left( \frac{\omega_{th}}{\omega_{^{129}\text{Xe}}} \right) \left( \frac{Q(\omega_{th})}{Q(\omega_{^{129}\text{Xe}})} \right) \end{aligned} \quad (4.19)$$

## 4.5 Results of Polarization Measurements by AFP

Polarization signals have been achieved multiple times in our lab. Samples of 5 atm 4:1 natural  $\text{Xe}$  to  $\text{N}_2$  are used for most of polarization runs. Fig. 4.4 shows the first AFP signal obtained from our lab. To calculate the polarization level, a proton signal must be measured. Tab. 4.1 lists data from a thermal proton signal

Parameter	$^1\text{H}$	error	$^{129}\text{Xe}$	error
$V_{signal}$	11 $\mu\text{V}$	5%	182 $\mu\text{V}$	5%
$\gamma$	$26.75 \times 10^7 \text{ T}^{-1}\text{s}^{-1}$	$\ll 1\%$	$7.45 \times 10^7 \text{ T}^{-1}\text{s}^{-1}$	$\ll 1\%$
$\rho$ (25 $^\circ\text{C}$ )	0.11 mol/cm <sup>3</sup>	$\ll 1\%$	$2.04 \times 10^{-5}$ mol/cm <sup>3</sup>	1 %
$\nu_0 (= \frac{\omega_0}{2\pi})$	92.00 kHz	$\ll 1\%$	35.00 kHz	$\ll 1\%$
$R_{probe}$	9.5 mm	5%	11 mm	5%
$Q(\omega)$	102.5 mV	5%	5.64 mV	5%
$G_{preamp}$	20	5%	50	5%
$P$	$6.99 \times 10^{-9}$	1%	$2.8 \times 10^{-2}$	10%

Table 4.1: Typical AFP Polarization Parameters

and the first hyperpolarization signal. The first signal obtained was about 3%, but subsequent polarization levels have been as high as 5%.

## 4.6 Results of Polarization Measurements by Pulsed NMR

Fig. 4.5 shows one of the four thermal signals measured in the Fraser MRI Lab. To get a signal with a high enough SNR, 5000 to 24000 signals are averaged. The thermal sample contained 8 atm 7:1 natural  $Xe$  to  $O_2$ . Fig. 4.6 shows the hyperpolarized signal obtained in the Fraser MRI Lab. That particular sample had 2.5 atm 4:1 natural  $Xe$  to  $N_2$ . The absolute value of the signal size is not available because the scales were not recorded. Therefore the average per scan peak to peak noise level is assumed to be constant, so the SNRs can be compared. The overall averaged noise and signal can be measured off the plots. However, the averaging of the scans must be taken into account. For the thermal polarization, it is assumed that the polarization signal is not changing much with time. This means that no corrections need to be made to the signal height due to averaging. The noise is a different story. After  $n$  averages, the overall averaged noise is a factor of  $\sqrt{n}$  smaller than the average per scan peak to peak amplitude of the noise:

Parameter	Thermal	error	Hyperpolarized	error
$n_{avg}$	24000	-	24	-
$\alpha$	10°	(est.)	10°	(est.)
$\beta$	-	-	0.83	(est.)
$\langle S \rangle$	11.5 mm	5%	34.0 mm	5%
$S_0$	11.5 mm	5%	43.3 mm	5%
$\langle N \rangle$	4.0 mm	10%	7.0 mm	10%
$N_{pkpk}$	620 mm	10%	34.3 mm	10%
$SNR$	0.019	10%	1.3	10%
$\rho$ (25 °C)	38 mol/m <sup>3</sup>	10%	10 mol/m <sup>3</sup>	5%
$P$	$1.76 \times 10^{-6}$	1%	$4.7 \times 10^{-4}$	20%

Table 4.2: Pulsed NMR Measurement Parameters

$$\langle N_{pkpk} \rangle = \frac{N_{1pkpk}}{\sqrt{n_{avg}}} \quad (4.20)$$

The signal for the hyperpolarized sample is affected by the averaging since each sweep destroys some of the polarization. Assuming that the total time to take the measurement is much shorter than the relaxation time of the sample, then the average magnetization is dependant only on parameter  $\beta$ :

$$\langle M \rangle = M_0 \frac{\sum_{j=1}^n \cos^n(\alpha)}{n} = \beta M_0 \quad (4.21)$$

Therefore it is important to know the tipping angle  $\alpha$ . The exact tipping angle for either measurement is not known, because the proper calibrations for  $Xe$  have not been done yet. I estimate it to be about 10° for both measurements because that is a fairly angle used. Given an angle of 10°,  $\beta$  is 0.83 for n=24. For comparison a tipping angle of 20° yields a  $\beta$  of 0.50 for n=24.

The denisty of the thermal probe has a large uncertainty because it was found

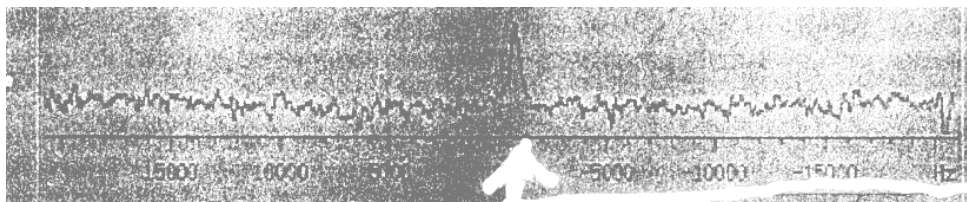


Figure 4.5: Thermal Xenon Signal (24k avg). The signal is seen above the white arrow.

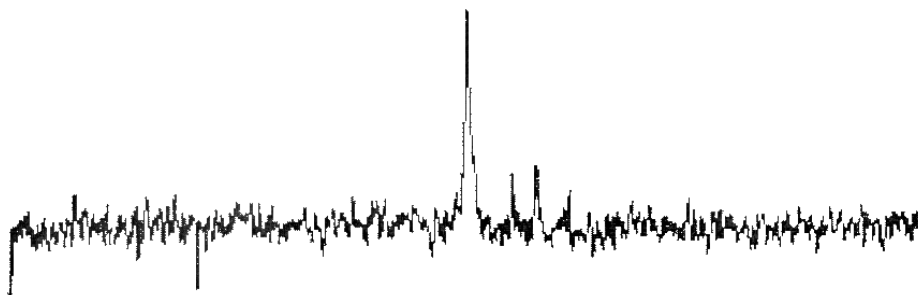


Figure 4.6: Hyperpolarized Xenon Signal (24 avg). This peak is distinguished from the thermal peak by (1) its narrower width and (2) its higher SNR.

that the probe is leaky at pressures above 4 atm. It should be noted that the signal heights for the four thermal measurements are all within 5%. This indicates that the probe had either (1) a negligible leak or (2) stopped leaking at a certain value. Therefore, for a worst case calculation, it will be assumed the probe was at 4 atm while the measurements were taken. The MR frequency of the two samples are different due to chemical shifting. Even if the  $O_2$  caused a chemical shift of 1000ppm, the corresponding frequency difference is less than 1%. Therefore the MR frequency ratio is very nearly 1. The capacitor tuning for the two runs were different, but they are meant to be tuned to frequencies around the MR frequency. Assuming the MR frequency is not on the steep part of the Q curve, then the ratio of the gains for the two frequencies should be on the order of 1. This results in a polarization level of about 0.05% which is a respectable improvement over thermal

polarization by a factor of about 250. Tab. 4.2 lists the parameters used for estimation of the polarization level attained in the Fraser MRI Lab.

## Chapter 5

### Conclusion

#### 5.1 Overview

This thesis project has been the beginning of the hyperpolarized  $^{129}\text{Xe}$  studies at Caltech & the hyperpolarized MRI collaboration with Prof. Scott Fraser. I have (1) demonstrated a cell design capable of being reused and producing large volumes of polarized  $^{129}\text{Xe}$ , (2) built and tested a gas system capable of characterizing & removing contaminants and filling cells, (3) demonstrated a successful delivery of polarized gas in the Fraser MRI Lab, (4) demonstrated polarization levels in our lab upto 5%, and (5) initiated studies involving frozen  $\text{Xe}$  delivery. In the following sections, I briefly review the two polarization experiments performed in the Fraser MRI Lab. I conclude with a list of possible future studies.

#### 5.2 Discussion of the Polarization Experiments

For comparison I briefly describe the set up and results from the measurements made in our lab. The range of polarizations measured in our lab is 3-5%. The cell and probe are connected directly by 31 cm PFA tubing. Therefore, these levels can be thought of as predelivery polarization levels. Most groups report polarizations of around 10%, so our numbers compare. The polarizations measured in Fraser MRI Lab is about 0.05%. The distance from the probe to the cell is about 310 cm; therefore, this polarization can be thought of as the post delivery level. This

signal measured is definitely a hyperpolarized signal. It cannot be a thermal signal because the peak is too narrow & large and the density of sample measured was too small. The peak is not noise because it was in the same place for 24 scans and it is the largest artifact on the averaged scan. The 0.05% value has a very large error associated with it, because many of the parameters used in the calculation had to be estimated. Note the this number is presented as the worst case level of polarization. All the other runs failed to produce a signal in the Fraser MRI Lab. The only common factor to all the failed runs was the fact that the O-rings on the valves failed some time during the run. During the first experiment, the broken O-rings were not noticed until after the last run. Before introducing the sample into the probe, the entire delivery line upto the cell valve is evacuated. If the O-ring failed before the evacuation, then the sample could have easily been pumped out and this is probably what happened.

During the second experiment, a few runs were taken without pumping out the delivery line in case of O-ring failure. While the sample is being polarized, the rest of the delivery line is held overpressured with  $N_2$ . If the O-ring did break during the pump, the sample would probably distribute itself throughout the delivery line via a diffusion process. All of the O-rings were broken when they were examined after the last run. The conclusion is that the samples were probably being polarized, but the polarization was lost (1) by being pumped out of the cell during the evacuation process or (2) diffusing out of the cell during the polarization process.

It is interesting to note that the O-rings only failed once in our lab. The air flow used in our lab to heat the cell is much faster than the air flow provided in the Fraser MRI Lab. The fact the O-rings broke on the side open to the cell means that the O-ring failure mechanism is probably stress caused by large temperature gradients to O-ring. The short term solution to this problem is to polarize the sample in our lab and then deliver it to the MRI lab via frozen transfer. This system what is currently being developed. The long term solution is to use a valve that is more resistant to temperature variations.

## 5.3 Future Areas of Research

This thesis project is only the first step in a long line of research involving both the large volume production of polarized  $Xe$  and imaging with  $Xe$ . The following is only a brief list of possible future research projects and improvements to system design.

### 5.3.1 Cell Wall Coatings

It has been known for a long time that various types of cell wall coatings can greatly decrease wall relaxation rates for both  $Rb$  and  $Xe$ . This ultimately leads to higher polarization levels of  $Xe$ . Two examples of coatings that have been successful in the past are  $RbH$  and a silicone based coating called SurfaSil. SurfaSil increases the relaxation time from many seconds to many minutes. Driehuys et al. [12] have determined that the dipolar coupling of the magnetic moments of surface protons and  $Xe$  nuclei is the dominant source of relaxation. There is a strong field dependence on this relaxation for fields up to about 40 gauss. Above 40 gauss the relaxation is basically field independent. The relaxation is also exponentially dependent on temperatures. It has been suggested that even longer relaxation times can be achieved by using deuterium instead of protons in the coating. The magnetic moment of deuterium is 6.5 times smaller than protons which would roughly correspond to an increase of relaxation times by a factor of 15. Another approach could be to make the coating less permeable to the  $Xe$  by fluorinating the coating compound. However the  $Rb$  vapor may react with the fluorination. Regardless, systematic studies must be performed to find the optimal coating.

### 5.3.2 $Cs$ Spin Exchange

Zeng et al. predict using  $Cs$  to polarize  $Xe$  may be better than  $Rb$  to  $Xe$  [46]. Recall that Wu et al. [45] predict that the spin rotation coupling parameter  $\gamma(R)$  between the alkali metal and noble gas is inversely proportional to the alkali metal mass and the interatomic separation.  $Cs$  is both heavier and larger than  $Rb$ . This indicates that

Parameter	Rb-Xe	Cs-Xe
$\gamma(R)/h$	$38 \pm 5$	$49 \pm 8$
$\alpha(R)/h$	$121 \pm 5$	$141 \pm 16$
x	0.31	0.35
$\frac{1}{x^2}$	9.6%	12%

Table 5.1: Comparison of Spin Exchange Parameters for Rb and Cs

the spin rotation coupling of *Cs* with *Xe* is weaker resulting in more efficient spin exchange. Walker's estimates [39] for values of  $\gamma(R)$  and  $\alpha(R)$  the spin exchange coupling parameter are located in Tab. 5.1. The parameter  $\frac{1}{x^2}$  gives a measure of the spin exchange efficiency. According to this model, *Cs-Xe* should be about 20% better than *Rb-Xe*. This would result in a higher *Xe* polarization. Initial studies have been performed by Levron et al. [24] indicating that it is possible to produce *Xe* polarization from *Cs* spin exchange. The wavelength needed for optical pumping of *Cs* (851 nm) is not readily available using diode laser technology, however it can be attained using  $\text{Ar}^+$  Ti:Sapphire array.

### 5.3.3 Improvement of Materials

As is mentioned before *Al* is slightly paramagnetic. Other nonparamagnetic materials should be considered. Unfortunately, many commonly available metals and alloys are paramagnetic or even worse ferrous. One possibility around this is to coat materials such as stainless steel with a relatively thick layer of a non paramagnetic substance. Another area of improvement is the glass being used. Using higher quality glass can result in less outgassing of impurities from the wall when the cell is heated. Teflon products work well except when in the presence of Rb. Perhaps they can be used in the storage of the sample after the Rb has been removed from it.

### 5.3.4 Other Considerations

The field gradients around the large Fraser MRI magnet may cause large relaxation. The relaxation could very well prove path dependant or dependant on the initial alignment of the spins. This is potential problem that should be studied in more detail. Using a frozen  $Xe$  delivery system lends itself well to this study because the spins could be delivered to the magnet in any orientation with respect to the field gradients. Gas ratios should be studied. An optimal gas mixture based on price and effective polarization should be sought. The price of the sample gas could one day be a limiting factor for the clinical use of hyperpolarized MRI.

## Appendix A

### Constant & Parameter Data Sheet

This section contains three tables. Table A.1 is a list of experimentally measured values for parameters relating to spin exchange and optical pumping. The data is included so that the reader can get a more tangible understanding for what the equations in Chapter 2 mean. The following abbreviations are used: VARCS - velocity averaged relaxation cross section, SE - spin exchange, PB - pressure broadening, Diff.- diffusion, Freq. - frequency. The VARCS for *Rb* and *Xe* collisions is not listed because I could find one. Table A.2 is a list of pressure conversions. This is include so that the section on the gas system is easier to understand. I often use many different units for pressure. Table A.3 is a list of nuclear data for *H*, *He*, *Rb*, and *Xe*. This is included as reference for comparison.

Parameter	Symbol	Value	Error	Units	Ref.
VARCS,Rb-Rb	$\langle v\sigma \rangle_{Rb-Rb}$	$8 \times 10^{-13}$	-	$\text{cm}^3\text{s}^{-1}$	[37]
VARCS,Rb-N <sub>2</sub>	$\langle v\sigma \rangle_{Rb-N_2}$	$8 \times 10^{-18}$	-	$\text{cm}^3\text{s}^{-1}$	[37]
VASECS,Rb-Xe	$\langle v\sigma \rangle_{Rb-Xe}$	$3.70 \times 10^{-27}$	0.70	$\text{cm}^3\text{s}^{-1}$	[10]
SE Parameter,3-body	$\gamma_M$	$2.92 \times 10^4$	0.59	$\text{s}^{-1}$	[10]
SE Constant,3-body	$\zeta$	0.1791	-	-	[10]
D1 Line, Rb	D1	794.76	-	nm	[48]
PB,Rb,D1,Xe	$D1\Gamma_{Xe}$	18.9	0.5	GHz/amg	[30]
PB,Rb,D1,N <sub>2</sub>	$D1\Gamma_{N_2}$	17.8	0.3	GHz/amg	[30]
VARCS,Xe-Xe	$\langle v\sigma \rangle_{Xe-Xe}$	$5 \times 10^{-6}$	-	sec·amg	[40]
Diff.Const.,Xe	D	0.06	-	$\text{cm}^2\text{s}^{-1}$	[8]
Freq. Shift Parameter	$\kappa_0$	650	5%	-	[25]

Table A.1: Parameters Relevant to Optical Pumping and Spin Exchange

	1 Pa	1 mbar	1 Torr	1 psi	1 atm
Pa =	1	100.00	133.3	$6.895 \times 10^3$	101325
mbar =	$1.000 \times 10^{-2}$	1	1.333	$6.895 \times 10^1$	1013.25
Torr =	$7.501 \times 10^{-3}$	0.7501	1	$5.171 \times 10^4$	760
psi =	$1.450 \times 10^{-4}$	0.0145	$1.934 \times 10^{-2}$	1	14.6959
atm =	$9.869 \times 10^{-4}$	0.9869	$1.318 \times 10^{-2}$	$6.805 \times 10^{-2}$	1

Table A.2: Pressure Conversions

Element	Atomic #	% Nat. Abn.	$I_N$	$\gamma(10^7 T^{-1} \cdot \text{s}^{-1})$	$\mu(\mu_N)$
Hydrogen	1	99.985	$\frac{1}{2}$	26.75221	4.83735
Helium	3	0.000137	$\frac{1}{2}$	-20.38016	-3.68515
Rubidium	85	72.165	$\frac{5}{2}$	2.59271	1.60131
Rubidium	87	27.835	$\frac{3}{2}$	8.78640	3.55258
Xenon	129	26.4	$\frac{1}{2}$	-7.45210	2.20908
Xenon	131	21.2	$\frac{3}{2}$	-1.34749	0.89320

Table A.3: Nuclear Data of Relevant Elements

## Appendix B

### Magnetic Resonance

#### B.1 Time Evolution of Spins in Static & Rotating Fields

The Hamiltonian of a particle with spin  $K$  in a static magnetic field  $B$  and a rotating perpendicular field  $B_1$  is:

$$H = \vec{\mu}_K \cdot (\vec{B} + \vec{B}_1(t)) = \gamma \vec{K} \cdot (B\hat{z} + B_1 \cos(\omega_0 t)\hat{x} + B_1 \sin(\omega_0 t)\hat{y}) \quad (\text{B.1})$$

For  $^{129}\text{Xe}$ ,  $K = \frac{1}{2}$  and if  $\hat{\sigma}$  is the vector form of the Pauli spin matrices, then:

$$\begin{aligned} \vec{K} &= \frac{\hbar}{2} \hat{\sigma} = \frac{\hbar}{2} (\sigma_x \hat{x} + \sigma_y \hat{y} + \sigma_z \hat{z}) \\ &= \frac{\hbar}{2} \left[ \begin{pmatrix} 0 & 1 \\ 1 & 0 \end{pmatrix} \hat{x} + \begin{pmatrix} 0 & -i \\ i & 0 \end{pmatrix} \hat{y} + \begin{pmatrix} 1 & 0 \\ 0 & -1 \end{pmatrix} \hat{z} \right] \end{aligned} \quad (\text{B.2})$$

Plugging into Schrodinger's eqn.,  $H\Psi = i\hbar \frac{\partial \Psi}{\partial t}$ :

$$\gamma \frac{\hbar}{2} \left[ B_1 \cos(\omega_0 t) \begin{pmatrix} \psi_2 \\ \psi_1 \end{pmatrix} + B_1 \sin(\omega_0 t) \begin{pmatrix} -i\psi_2 \\ i\psi_1 \end{pmatrix} + B \begin{pmatrix} \psi_1 \\ -\psi_2 \end{pmatrix} \right] = i\hbar \begin{pmatrix} \frac{\partial \psi_1}{\partial t} \\ \frac{\partial \psi_2}{\partial t} \end{pmatrix} \quad (\text{B.3})$$

Multiplying the matrices out, we get a pair of coupled first order differential eqns:

$$\begin{aligned}\frac{\partial\psi_1}{\partial t} &= -i \left[ \frac{\gamma B}{2} \psi_1 + \frac{\gamma B_1}{2} \psi_2 (\cos(\omega_0 t) - i \sin(\omega_0 t)) \right] \\ &= -i \left( \frac{\omega}{2} \psi_1 + \frac{\omega_1}{2} \psi_2 \exp(-i\omega_0 t) \right)\end{aligned}\tag{B.4}$$

$$\begin{aligned}\frac{\partial\psi_2}{\partial t} &= -i \left[ -\frac{\gamma B}{2} \psi_2 + \frac{\gamma B_1}{2} \psi_1 (\cos(\omega_0 t) + i \sin(\omega_0 t)) \right] \\ &= -i \left( -\frac{\omega}{2} \psi_2 + \frac{\omega_1}{2} \psi_1 \exp(+i\omega_0 t) \right)\end{aligned}\tag{B.5}$$

The following transformation switches the equation to a frame of reference that is co-rotating with  $B_1$ :

$$\psi_1 = \phi_1 \exp\left(-i\frac{\omega_0}{2}t\right)\tag{B.6}$$

$$\psi_2 = \phi_2 \exp\left(+i\frac{\omega_0}{2}t\right)\tag{B.7}$$

This gives us coupled first order differential equations that have only constant coefficients:

$$i\frac{\partial\phi_1}{\partial t} = -(\omega_0 - \omega)\phi_1 + \omega_1\phi_2\tag{B.8}$$

$$i\frac{\partial\phi_2}{\partial t} = (\omega_0 - \omega)\phi_2 + \omega_1\phi_1\tag{B.9}$$

The general solutions are readily found, still in the co-rotating frame:

$$\Psi = \left( \begin{array}{l} a_1 \exp\left[\frac{i}{2}\left(\sqrt{(\omega_0 - \omega)^2 + \omega_1^2}\right)t\right] + a_2 \exp\left[-\frac{i}{2}\left(\sqrt{(\omega_0 - \omega)^2 + \omega_1^2}\right)t\right] \\ b_1 \exp\left[\frac{i}{2}\left(\sqrt{(\omega_0 - \omega)^2 + \omega_1^2}\right)t\right] + b_2 \exp\left[-\frac{i}{2}\left(\sqrt{(\omega_0 - \omega)^2 + \omega_1^2}\right)t\right] \end{array} \right)\tag{B.10}$$

Assuming that we have 100% polarization such that all the spins are in the  $+\frac{1}{2}$  state at  $t = 0$ , then our state function becomes:

$$\Psi = \frac{\sin\left(\frac{t}{2}\sqrt{(\omega_0 - \omega)^2 + \omega_1^2}\right)}{\sqrt{(\omega_0 - \omega)^2 + \omega_1^2}} \cdot \begin{pmatrix} -\frac{i}{2}(\omega_0 - \omega) + \frac{1}{2}\sqrt{(\omega_0 - \omega)^2 + \omega_1^2} \cot\left(\frac{1}{2}\sqrt{(\omega_0 - \omega)^2 + \omega_1^2}\right) \\ \frac{i}{2}\omega_1 \end{pmatrix} \quad (\text{B.11})$$

The probability that the spins will flip from  $+\frac{1}{2}$  to  $-\frac{1}{2}$  at some time  $t$  is given as:

$$P(+ \rightarrow -) = |\langle - | \Psi \rangle|^2 = |\phi_2|^2 = \left(\frac{\omega_1^2}{(\omega_0 - \omega)^2 + \omega_1^2}\right) \sin^2\left(\frac{t}{2}\sqrt{(\omega_0 - \omega)^2 + \omega_1^2}\right) \quad (\text{B.12})$$

## B.2 Effective Field Felt by a Spin

We have shown that when a sample is in the presence of a magnetic field, the individual spins of the sample begin to precess about the field at the Larmor frequency given as:

$$\omega = \gamma B \quad (\text{B.13})$$

Note that the frequencies being discussed are *angular* frequencies  $\omega$  and not *temporal* frequencies  $\nu$ . These are related by:

$$\omega = 2\pi\nu \quad (\text{B.14})$$

Suppose now that a rotating field of frequency  $\omega_0$  and magnitude  $B_1$  is applied transverse to the holding field  $\vec{B}$ . The total field is then:

$$\vec{B}_{tot} = B_1 \cos(\omega_0 t) \hat{x} + B_1 \sin(\omega_0 t) \hat{y} + B \hat{z} \quad (\text{B.15})$$

By Ehrenfest's principle, this situation can be analyzed classically if the expectation values or averages of the relevant parameters are used. Therefore the average magnetic moment of the spins is:

$$\langle \vec{\mu} \rangle = \gamma \langle \vec{S} \rangle \quad (\text{B.16})$$

$\langle S \rangle$  is the average spin angular momentum of the spins. The torque that each spin experiences due to  $\vec{B}_{tot}$  is:

$$\frac{d \langle \vec{S} \rangle}{dt} = \langle \vec{\mu} \rangle \times \vec{B}_{tot} = \gamma \langle \vec{S} \rangle \times (B_1 \cos(\omega_0 t) \hat{x} + B_1 \sin(\omega_0 t) \hat{y} + B \hat{z}) \quad (\text{B.17})$$

The analysis is made easier if this equation is transformed into a frame that is co-rotating in the same direction and about the same axis as the precession of the spins, but with a frequency of  $\omega_0$ . The following relation is handy:

$$\left[ \frac{d \langle \vec{S} \rangle}{dt} \right]_{rot} = \frac{d \langle \vec{S} \rangle}{dt} + \vec{\omega}_0 \times \langle \vec{S} \rangle \quad (\text{B.18})$$

Transforming  $\vec{B}_{tot}$  into this rotating frame and combining the two previous equations:

$$\begin{aligned} \left[ \frac{d\langle \vec{S} \rangle}{dt} \right]_{rot} &= \gamma \langle \vec{S} \rangle \times (B_1 \hat{x}_{rot} + B \hat{z}) - \vec{\omega}_0 \times \langle \vec{S} \rangle \\ &= \gamma \langle \vec{S} \rangle \times \left[ \left( B - \frac{\omega_0}{\gamma} \right) \hat{z} + B_1 \hat{x}_{rot} \right] \end{aligned} \quad (\text{B.19})$$

where,

$$\hat{x}_{rot} = \cos(\omega_0 t) \hat{x} + \sin(\omega_0 t) \hat{y} \quad (\text{B.20})$$

Therefore the effective field felt by the spin is:

$$\vec{B}_{eff}(t) = \left( B(t) - \frac{\omega_0}{\gamma} \right) \hat{z} + B_1 \hat{x}_{rot} \quad (\text{B.21})$$

### B.3 Signal Induced by Spin Flip

All magnetic resonance phenomenon depend on the ideas put forth in the previous two sections. It is important to note that these relations dictate the time evolution of individual spins. In real life, one studies an ensemble of spins by measuring the magnetization of the sample:

$$\vec{M} = \mu \rho P \hat{B}_{eff}(t)$$

where  $\mu$  is the magnetic moment of the spin,  $\rho$  is the density of the spin,  $P$  is the polarization of the sample. Note the magnetization points in the direction of the effective field. The signal produced in a set of pickup coils mutually orthogonal to

the holding field  $\vec{B}$  and the rotating field  $\vec{B}_1$  is given by Faraday's Law:

$$S(t) = \left| \frac{d\Phi_M}{dt} \right| = \left| \frac{d \int \vec{M}(t) \bullet d\vec{a}}{dt} \right| \quad (\text{B.22})$$

Assuming that the coils are ideal, meaning they are perfectly flat and have zero thickness, the signal is:

$$S(t) = \mu\rho P \left| \frac{d \int \hat{B}_{eff}(t) \bullet d\vec{a}}{dt} \right| \quad (\text{B.23})$$

The signal produced is proportional only to the transverse component of the  $\vec{M}$ :

$$\vec{M}_{trans} = \frac{B_1 \cos(\omega_0 t)}{\sqrt{\left(B(t) - \frac{\omega_0}{\gamma}\right)^2 + B_1^2}} \quad (\text{B.24})$$

If we assume that the magnetic fields applied to the sample are perfectly uniform, the integral and derivative can be separated:

$$S = \mu\rho P \int da \left| \frac{d \left( \frac{B_1 \cos(\omega_0 t)}{\sqrt{\left(B(t) - \frac{\omega_0}{\gamma}\right)^2 + B_1^2}} \right)}{dt} \right| \quad (\text{B.25})$$

Carrying out the integration, assuming that the sample completely fills the volume in between the coils, and the differentiation, we get:

$$\begin{aligned}
S(t) = & \mu\rho P \frac{\omega_0 B_1 A \sin(\omega_0 t)}{\sqrt{\left(B(t) - \frac{\omega_0}{\gamma}\right)^2 + B_1^2}} \\
& - \mu\rho P \omega_0 B_1 A \cos(\omega_0 t) \left( \left(B(t) - \frac{\omega_0}{\gamma}\right)^2 + B_1^2 \right)^{-\frac{3}{2}} \left(B(t) - \frac{\omega_0}{\gamma}\right) \frac{dB(t)}{dt}
\end{aligned} \tag{B.26}$$

where  $A$  is the area of the coils. Close to resonance, the signal shape (per unit volume) is given as:

$$S(t) \approx \omega_0 \mu\rho P A \frac{B_1 \sin(\omega_0 t)}{\sqrt{\left(B(t) - \frac{\omega_0}{\gamma}\right)^2 + B_1^2}} \tag{B.27}$$

The assumptions made to get to this result are close enough to reality for this solution to be a good indicator of what parameters the signal depends on.

## Appendix C

### Dynamics of $Xe$ in a Biological Environment

#### C.1 Overview

This appendix is meant to review some of the current work dealing with the biological applications of hyperpolarized  $^{129}Xe$ . Specifically discussed are those topics that will become important when imaging studies commence. Delivery via ventilation and injection are described and compared. A basic outline of the uptake process based on the work of Martin et al. [26] is presented. The biggest obstacle to hyperpolarized imaging is the relatively short time scale over which the polarization is measurable. Hence, I conclude with a review of the relaxation times measured in various biological settings.

#### C.2 Delivery by Ventilation

Polarized  $Xe$  is introduced to the biological sample by ventilation or injection. The standard technique thus far has been ventilation. The relative ease and non-invasiveness of this technique are its main advantages. For rats and mice, an animal respirator is used to supply the polarized  $Xe$ . For humans, the gas is collected in a bag and then quickly inhaled by the patient. In two experiments conducted by Wagshul et al. [38] & Rosen et al. [33], a mouse was supplied with 2-3cc of gas over a 40-60s period with a breathing rate of 65-80bpm. This gives an upper limit of about 240cc of gas used per minute. Various gas mixtures were used in

Carrier	Solubility	$T_1$ (in blood, otherwise noted)
Blood	0.18	5 s
Saline	0.09	5 s
Intralipid (20%)	0.40	16 s
Perfluorooctyl bromide (PFOB) (20%)	0.22	34 s in RBC, 67 s in PFOB

Table C.1: Injectable Carrier Parameters

those experiments. High ratios of  $Xe$  to  $O_2$  can cause undesirable anoxic ( $>1$ ) and anaesthetic ( $>2.5$ ) effects. It is well known that a fractional concentration of 0.35  $Xe$  in a gas mixture is safe and has nonanesthetic effects for humans as well as for mice. I suggest therefore that a ratio of  $Xe$  to  $O_2$  of around 0.5 is used. This corresponds to about 80cc of  $Xe$ . To maximize the signal, it is also suggested that enriched (70% to 80%)  $Xe$  is used as opposed to natural abundance  $Xe$ .  $O_2$  is introduced into the gas mixture immediately before the mouse breathes in the gas. This insures that the mouse maintains safe levels of oxygenation and minimizes the amount of spin relaxation due to the paramagnetic  $O_2$ . Using this procedure typically requires a tracheotomy and subsequent euthanization of the mouse.

### C.3 Delivery by Injection

Injection delivery offers many advantages although intrusive. It saves valuable time by removing the transit time from the heart to the target organ when ventilated. It minimizes the volume of  $Xe$  and allows for the isolation of the target tissue. The  $Xe$  gas is dissolved into solution by overpressuring the solution. It is then injected into the mouse through a catheter. The difficulty in this method is finding the proper solution to dissolve the  $Xe$ . Goodson [17] reports the properties of potential noble gas carriers. A table adapted from [17] is listed in Tab. C.1. The solubility quoted is the Ostwald solubility which is the STP volume of gas dissolved in 1 L of solution at 1 atm gas pressure.

The  $T_1$  of  $Xe$  in saline is not any better than for blood. Intralipid, an aqueous

suspension of lipid vesicles, is a good choice because it is known to be safe biologically and it can easily dissolve  $Xe$ . PFOB is an interesting possibility first suggested by Wolber et al. [44]. It is a type of perfluorocarbon compound which is known to dissolve  $CO_2$  and  $O_2$  and therefore is a popular candidate for a blood substitute. Pure samples of this carrier have exceedingly high solubilities and relaxation times. Unfortunately, PFOB has to be emulsified upto the point that its droplet size is comparable to that of a red blood cell (RBC) in order to facilitate absorption into tissue.

## C.4 $Xe$ Uptake Models

Various models of  $Xe$  uptake have been proposed. They all have the same basic steps. 1)  $Xe$  is ventilated into the lungs. 2)  $Xe$  enters the blood stream by diffusion on the order of 1 s. 3) It is pumped through the heart to various organs in the body including the brain (on the order of 1 s for mice and 5 s for humans). 4) Finally the  $Xe$  collects in areas that are lipid rich such as the fat surrounding various tissues. In the brain, it has been shown that the  $Xe$  resides mainly in the cerebrum. A model by Martin et al. [26] predicts that after about 30s the relative concentration of  $Xe$  vs. arterial concentrations of  $Xe$  in the cerebral tissue will reach a steady state value, if  $Xe$  is being constantly supplied via ventilation. Work by Swanson et al. [36] more or less agrees with this theoretical predication and they indicate that even after the blood resonances had disappeared, the tissue and fat resonances remain.

## C.5 Relaxation in Various Tissues

Relaxation times of  $Xe$  of various tissues have been measured *in vitro* (see Tab. C.2).

In blood that has been allowed to sediment, two peaks appear having different relaxation times. These peaks are for RBCs and plasma and their relaxation times differ by about 5 s. However, *in vivo* RBCs and plasma are undergoing a rapid  $Xe$

<b>Tissue/Organ</b>	$T_1^*$	$B_o$	<b>Source</b>	<b>Ref.</b>
RBC	4.5s	2.35T	Thermal	[2]
Plasma	9.6s	2.35T	Thermal	[2]
Arterial blood levels of oxygenation	6.4s	1.5T	HypXe	[43]
Venous blood levels of oxygenation	4.0s	1.5T	HypXe	[43]
Deoxygenated blood	4.0s	1.5T	HypXe	[4]
Oxygenated blood	13.5s	1.5T	HypXe	[4]
Brain oxy(deoxy)	18s(22s)	9.4T	HypXe	[42]
Kidney oxy(deoxy)	7.3s(10.0s)	9.4T	HypXe	[42]
Liver oxy(deoxy)	6.1s(8.1s)	9.4T	HypXe	[42]
Lung oxy(deoxy)	6.2s(4.4s)	9.4T	HypXe	[42]

Table C.2: Relaxation Times

exchange on the order of 12 ms. Therefore the expected and experimentally verified results is a single peak with a relaxation time of about 6 s. Albert et al. [4] & Wolber et al. [43] have reported a dependance of the relaxation time to the level of oxygenation of the blood. It was originally thought that deoxygenated blood would have a longer  $T_1$ , because free  $O_2$  in the plasma was thought to dominate the relaxation. However, it was found that oxygenated blood had relaxation times of almost twice as long. This indicates that deoxyhemoglobin is the dominant relaxation agent. With this in mind it is noted that the ratio of bound  $O_2$  to free  $O_2$  in the blood is about 100 to 1 at physiological levels of oxygenation. The dependance of  $T_1$  to the level of oxygenation is thought to come from structural differences between deoxyhemoglobin and oxyhemoglobin. It has been shown that deoxyhemoglobin is paramagnetic, while oxyhemoglobin has zero magnetic moment [4]. Also, the binding sites for  $Xe$  may be different for the two species of hemoglobin. Incidentally, the binding of  $Xe$  to hemoglobin is due mainly to Debye and London interactions (van der Waals forces).

## Bibliography

- [1] Albert MS, Cates CD, Driehuys B, Happer W, Saam B, Springer Jr CS, Wishnia A. Biological magnetic resonance imaging using laser-polarized  $^{129}\text{Xe}$ . *Nature* 1994: Vol.370, p199-201.
- [2] Albert MS, Schepkin VD, Budinger TF. Measurement of the  $^{129}\text{Xe}$   $T_1$  in Blood to Explore the Feasibility of Hyperpolarized  $^{129}\text{Xe}$  MRI. *Journal of Computer Assisted Tomography* 1995: Vol.19(6), p975-8.
- [3] Albert MS, Balamore D. Development of hyperpolarized noble gas MRI. *Nuclear Instruments & Methods in Physics Research A* 1998: 402, p441-53.
- [4] Albert MS, Kacher DF, Balamore D, Venkatesh AK, Jolesz FA.  $T_1$  of  $^{129}\text{Xe}$  in Blood and the Role of Oxygenation. *Journal of Magnetic Resonance* 1999: 140, p264-73.
- [5] Appelt S, Baranga AB, Erickson CJ, Romalis MV, Young AR, Happer W. Theory of spin-exchange optical pumping of  $^3\text{He}$  and  $^{129}\text{Xe}$ . *Physical Review A* 1998: Vol.58(2), p1412-39.
- [6] Bifone A, Song YQ, Seydoux R, Taylor RE, Goodson BM, Pietrass T, Budfinger TF, Navon G, Pines A. NMR of laser-polarized xenon in human blood. *Proc. Natl. Acad. Sci. USA* 1996: Vol.93, p12932-6.
- [7] Bouchiat MA, Carver TR, Varnum CM. Nuclear polarization in  $^3\text{He}$  gas induced by optical pumping and dipolar exchange. *Physical Review Letters* 1960: 5, p373-5.

- [8] Brunner E. Enhancement of Surface and Biological Magnetic Resonance Using Laser-Polarized Noble Gases. *Concepts in Magnetic Resonance* 1999: Vol.11(5), p313-35.
- [9] Cates GD, White DJ, Chien TR, Schaefer SR, Happer W. Spin relaxation in gases due to inhomogeneous static and oscillating magnetic fields. *Physical Review A* 1990: Vol.38(10), p5092-106.
- [10] Cates GD, Fitzgerald RJ, Barton AS, Bogorad P, Gatzke M, Newbury NR, Saam B. *Rb-<sup>129</sup>Xe* spin-exchange rates due to binary and three-body collisions at high *Xe* pressures. *Physical Review A* 1992: Vol.45(7), p4631-9.
- [11] Chupp TE, Swanson SD. Medical Imaging with Laser Polarized Noble Gases. Preprint, 2000. (available at <http://www.physics.lsa.umich.edu/chupp/LasPolNobGasImagPreprint.pdf>)
- [12] Driehuys B, Cates GD, Happer W. Surface Relaxation Mechanisms of Laser-Polarized <sup>129</sup>Xe. *Physical Review Letters* 1995: Vol.74(24), 4943-6.
- [13] Fitzgerald RJ, Gatzke M, Fox DC, Cates GD, Happer W. <sup>129</sup>Xe spin relaxation in frozen xenon. *Physical Review B* 1999: Vol.59(13), p.8795-811.
- [14] Gao J, Lemen L, Xiong J, Patyal B, Fox PT. Magnetization and Diffusion Effects in NMR Imaging of Hyperpolarized Substances. *Magnetic Resonance in Medicine* 1997: 37, p153-8.
- [15] Gatzke M, Cates GD, Driehuys B, Fox D, Happer W, Saam B. Extraordinarily Slow Nuclear Spin Relaxation in Frozen Laser-Polarized <sup>129</sup>Xe. *Physical Review Letters* 1993: Vol70(5), p690-3.
- [16] Goodson BM, Song YQ, Taylor RE, Schepkin VD, Brennan KM, Chingas GC, Budfinger TF, Navon G, Pines A. In vivo NMR and MRI using injection delivery of laser-polarized xenon. *Proc. Natl. Acad. Sci. USA* 1997: Vol.94, p14725-9.
- [17] Goodson, BM. Using Injectable Carriers of Laser-Polarized Noble Gases for

- Enhancing NMR and MRI. Concepts in Magnetic Resonance 1999: Vol.11(4), p203-23.
- [18] Grover BC. Noble-gas NMR detection through noble-gas-rubidium hyperfine contact interaction. Physical Review Letters 1978: 40, p391-2.
- [19] Happer W. Optical Pumping. Review of Modern Physics 1972: Vol.44(2), p169-249.
- [20] Hasson KC, Cates GD, Lerman K, Bogorad P, Happer W. Spin relaxation due to magnetic-field inhomogeneities: Quartic dependence and diffusion-constant measurements. Physical Review A 1990: Vol.41(7), p3672-88.
- [21] Herman RM. Theory of Spin Exchange Between Optically Pumped Rb and Foreign Gas Nuclei. Physical Review A 1965: 137, p1062-5.
- [22] Kastler A. Quelques suggestions concernant la production optique et la détection optique d'une inégalité de population des niveaux de quantification spatiale des atomes. Application a l'expérience de Stern Gerlach et la résonance magnétique. Journal de Physics Radium 1950: 11, p255-65.
- [23] Kauczor HU, Surkau R, Roberts T. MRI using hyperpolarized gases. European Radiology 1998: 8, p820-7.
- [24] Levron D, Walter DK, Appelt S, Fitzgerald RJ, Kahn D, Korbly SE, Sauer KL, Happer W, Earles TL, Mawst LJ, Botez D, Harvey M, DiMarco L, Connolly JC, Moller, *He*, Chen XJ, Cofer GP, Johnson GA. Magnetic resonance imaging of hyperpolarized  $^{129}\text{Xe}$  produced by spin exchange with diode-laser pumped Cs. Applied Physics Letters 1998: Vol.73(18), p2666-8.
- [25] Mabuchi, H. Wall Relaxation Mechanisms for Polarized Noble Gases. Princeton Senior Thesis 1992.
- [26] Martin CC, Williams RF, Gao J, Nickerson LDH, Xiong J, Fox PT. The Pharmacokinetics of Hyperpolarized Xenon: Implications for Cerebral MRI. Journal of Magnetic Resonance Imaging 1997: Vol.7(5), p848-54.

- [27] Middleton, HL. The Spin Structure of the Neutron Determined Using a Polarized  $^3\text{He}$  Target. Princeton Ph.D. Thesis 1994.
- [28] Mugler III JP, et al. MR Imaging and Spectroscopy Using Hyperpolarized  $^{129}\text{Xe}$  Gas: Preliminary Human Results. *Magnetic Resonance in Medicine* 1997: 37, 809-15.
- [29] Peled S, Jolesz FA, Tseng C, Nascimben L, Albert MS, Walsworth RL. Determinants of Tissue Delivery for  $^{129}\text{Xe}$  Magnetic Resonance in Humans. *Magnetic Resonance in Medicine* 1996: 36, 340-4.
- [30] Romalis MV, Miron E, Cates GD. Pressure broadening of  $Rb$   $D_1$  and  $D_2$  lines by  $^3\text{He}$ ,  $^4\text{He}$ ,  $N_2$ , and  $Xe$ : Line cores and near wings. *Physical Review A* 1997: Vol.56(6), p4569-78.
- [31] Romalis, MV. Laser Polarized  $^3\text{He}$  Target Used for a Precision Measurement of the Neutron Spin Structure. Princeton Ph.D. Thesis 1997.
- [32] Romalis MV, Cates GD. Accurate  $^3\text{He}$  polarimetry using the  $Rb$  frequency shift due to the  $Rb-^3\text{He}$  spin-exchange collisions. *Physical Review A* 1998: Vol.58(4), p3004-11.
- [33] Rosen MS, Chupp TE, Coulter KP, Welsh RC, Swanson SD. Polarized  $^{129}\text{Xe}$  optical pumping/spin exchange and delivery system for magnetic resonance spectroscopy and imaging studies. *Review of Scientific Instruments* 1999: Vol.70(2), p1546-52.
- [34] Song Y, Goodson BM, Pines A. NMR and MRI Using Laser-Polarized Xenon. *Spectroscopy* 1999: Vol.14(7), p26-33.
- [35] Swanson SD, Rosen MS, Agranoff BW, Coulter KP, Welsh RC, Chupp TE. Brain MRI with Laser-Polarized  $^{129}\text{Xe}$ . *Magnetic Resonance in Medicine* 1997: 38, p695-8.
- [36] Swanson SD, Rosen MS, Coulter KP, Welsh RC, Chupp TE. Distribution and

- Dynamics of Laser-Polarized  $^{129}\text{Xe}$  Magnetization In Vivo. *Magnetic Resonance in Medicine* 1999: 42, p1137-45.
- [37] Wagshul ME, Chupp TE. Laser Optical-Pumping of High-Density *Rb* in Polarized *He-3* Targets. *Physical Review A* 1994: 49, p3854.
- [38] Wagshul ME, Button TM, Li HF, Liang Z, Springer CS, Zhong K, Wishnia A. In Vivo MR Imaging and Spectroscopy Using Hyperpolarized  $^{129}\text{Xe}$ . *Magnetic Resonance in Medicine* 1996: 36, p183-91.
- [39] Walker TG. Estimates of spin-exchange parameters of alkali-metal–noble gas pairs. *Physical Review A* 1989: vol.40(9), p4959-63.
- [40] Walker TG, Happer W. Spin-exchange optical pumping of noble-gas nuclei. *Review of Modern Physics* 1997, Vol.69(2), p629-42.
- [41] Welsh RC, Chupp TE, Coulter KP, Rosen MS, Swanson SD, Arganoff BW. Magnetic Resonance Imaging with laser-polarized  $^{129}\text{Xe}$ . *Nuclear Instruments & Methods In Physics Research A* 1998: 402, p461-3.
- [42] Wilson GJ, Santyr GE, Anderson ME, DeLuca Jr. PM. Longitudinal Relaxation Times of  $^{129}\text{Xe}$  in Rat Tissue Homogenates at 9.4T. *Magnetic Resonance in Medicine* 1999: 41, p933-8.
- [43] Wolber J, Cherubini A, Dzik-Jurasz ASK, Leach MO, Bifone A. Spin-lattice relaxation of laser-polarized xenon in human blood. *Proc. Natl. Acad. Sci. USA* 1999: Vol.96, p3664-9.
- [44] Wolber J, Rowland IJ, Leach MO, Bifone A. Perfluorocarbon Emulsions as Intravenous Delivery Media for Hyperpolarized Xenon. *Magnetic Resonance in Medicine* 1999: 41, p442-9.
- [45] Wu Z, Walker TG, Happer W. Spin-Rotation Interaction of Noble-Gas Alkali-Metal Atom Pairs. *Physical Review Letters* 1985: Vol.54(17), p1921-4.

- [46] Zeng X, Wu Z, Call T, Miron E, Schreiber D, Happer W. Experimental determination of the rate constants for the spin exchange between optically pumped K, Rb, and Cs atoms and  $^{129}\text{Xe}$  nuclei in alkali-metal–noble-gas van der Waals molecules. *Physical Review A* 1985: Vol.31(1), p260-78.
- [47] <http://www.webelements.com/>
- [48] <http://physics.nist.gov/PhysRefData/contents.html>